Structural assessment and seismic vulnerability of earthen historic structures. Application of sophisticated numerical and simple analytical models.

Georgios Karanikoloudis [a]*, Paulo B. Lourenço[b]

[a] ISISE, Department of Civil Engineering, University of Minho, Guimarães, Portugal

[b] ISISE, Department of Civil Engineering, University of Minho, Guimarães, Portugal

* Correspondence to Georgios Karanikoloudis, ISISE, Department of Civil Engineering, University of Minho, Campus de Azurém, Guimarães, 4800-058, Portugal; E-mail: karanikoloudis@hotmail.com; Tel: +351 912 258 827

Abstract: Adobe constructions account for a significant portion of the built heritage, associated with early building techniques, material accessibility and low-cost. Nonetheless, adobe buildings, due to their low mechanical properties and overturning resistance, are subject to early structural damage, such as cracking, separation of structural elements and, possibly, collapse in areas of high seismic hazard. The lack of maintenance and absence of adequate retrofitting techniques usually intensifies the loss of historic fabric. The current paper, aims at the structural assessment and seismic safety, in current conditions, of the Church of Kuño Tambo, a religious adobe structure of the 17th century, in Cusco region, in Peru. The inspection and diagnosis involved sonic testing and damage mapping, while ambient vibration tests revealed the modal response of the structure. The assessment of seismic vulnerability, together with the necessity of retrofitting measures were verified through nonlinear static and pushover parametric analyses, complemented with a macro-block limit analysis and a performance based assessment, under local seismic criteria. A more realistic response from dynamically induced ground motions was performed, by a nonlinear time history analysis, according to the Eurocode 8 framework. Through an integrated approach, in situ inspection, testing, numerical and

analytical modelling are associated under the scope of reproducing the existing structural damage, the sequence of inelastic behavior and verification of the necessity of retrofitting measures.

Keywords: Adobe historic constructions; Seismic vulnerability; Structural assessment; Nonlinear pushover analysis; Nonlinear dynamic analysis; Damage survey; Sonic tests; Dynamic identification tests; Limit analysis; Homogeneous modelling approach; Displacement based approach.

Short Title: Seismic vulnerability of earthen historic structures

1. Introduction

Adobe is one of the oldest and most widely used natural materials, which accounts for a significant part of the built heritage. In general, the overall seismic performance of masonry buildings is highly related to the level of redistribution of seismic loads between vertical elements [Lourenco et al. 2011]. The presence of good interlocking in connections, stiff floors, ring beams, tie beams and corner keys can provide a diaphragmatic behavior or structural integrity, also known as "box behavior", which can enhance a global structural response and redistribute seismic loads between vertical elements, in the different in-plane directions [Lourenco et al. 2011]. Adobe historic buildings, often lack this level of connection, and the corresponding structural damage is composed of in-plane failure in parts of the skeleton (rocking, sliding, diagonal tension and toe crushing), as well as out-of-plane, which is usually critical. The out-of-plane failure propagates in rotation planes, formed under flexural hinge lines, mostly in the interface between adobe and a masonry base course, due to the lower strength of adobe or on intermediate heights [Lourenco et al. 2011, Tolles et al. 1996]. Often, aspects, such as the lack of maintenance can escalate the degradation process, either chemical, physical or mechanical, leading to a reduction of long-term structural performance and durability [Angelillo M. et al. 2014].

The main structural characteristics of adobe historic structures, in terms of seismic vulnerability and corresponding damage, are mainly influenced by the large inertia forces (due to heavy and thick walls), the low mechanical properties (in tension and compression) and limited ductility. In the absence of internal or external bracing and given the magnitude and direction of the inertial forces, the connections between structural parts are considered insufficient, and the critical out-of-plane resistance is usually governed by the rigid body motion of individual walls [Lourenco et al. 2011, Varum et al. 2014, Tolles et al 1996]. In the presence of additional lateral restraint from buttresses and given the level of connectivity of intersecting

walls, out-of-plane mechanisms can involve smaller portions of the walls. The lateral resistance is related to the compressive strength of adobe masonry and to the effective compressive area of the cross-section, which counteracts the inertia destabilizing forces [Tomazevic 1999]. Thus, the compressed part of the rotation plane is often crushed under compression (toe crushing) ["OPCM 3431" 2005, "NTC" 2008]. Yet, in specific adobe historic structures, composed by walls of large width and low in height, the compressive strength is not much influencing the maximum load capacity, as shown in this work. Adobe structures have a compressive strength in the range 0.5-3 MPa, with the modulus of elasticity being usually lower than 1 GPa, thus experiencing high deformations and relatively brittle failures ["NIKER" 2010].

When box behavior is present, out-of-plane vertical cracks can still be formed, due to bending at the corners and in the middle of the walls. But, in-plane bending and mostly shear, cause horizontal, vertical and diagonal cracks. Damage mechanisms depend mainly on the geometry of the wall (height/width ratio), boundary conditions and additional vertical loading.

The presence of discontinuities and openings are also influential, with shear cracks forming in the proximity of spandrel beams and at the corners of openings. In-plane damage can also be the result of interaction or rocking, under seismic excitation, between structural elements of different stiffness, such as the main facades of Cathedrals when circumscribed between bell towers.

The current study discusses the structural performance and seismic assessment of the Church of Santiago Apóstol de Kuño Tambo, in Acomayo, Cusco, in Peru and is part of the Seismic Retrofitting Project (SRP) of the Getty Conservation Institute (GCI), USA. The correlation with the existing structural damage and the structural capacity were obtained through nonlinear pushover and time history analyses, based on a macro-modeling approach, with a total rotating strain crack model, with compressive and tensile softening behavior, incorporating fracture energy [Lourenco 1998]. Capacity curves of lateral resistance and

vectorial-time history plots, corresponding with local failure modes, have been compared with the local seismic capacity demand of the Peruvian seismic code of 0.25g ["NTE-0.30" 2016].

The uncertainty of confinement provided by the system of anchored ties existing in the structure was accounted, by conducting pushover analyses with no ties and with ties anchored to the external part of the lateral walls. The assigned material properties were retrieved from the experimental campaign provided by the GCI, the onsite testing campaign, conducted by the University of Minho in May 2015, and from literature [Greco et al. 2015, "SRP" 2014].

2. Description of the building and damage identification

The church of Kuño Tambo is a religious structure of the 17th century (1681), representative of churches built in the Andes, during the Spanish Viceroyalty period (Figure 1). Its historic significance lays in the limited number of past interventions, and the mural paintings present in the interior finishes. It consists of a single nave, leading to an elevated Presbytery and Altar, with an adjacent sacristy and baptistery (Figure 2). The walls and buttresses are of adobe masonry, with a single gable timber roof and a roof cover composed of canes, a layer of mud and straw, and clay roof tiles. The trusses are weakly connected to a ridge beam on top (small cross-section and non-continuous). The joists, made by leather straps, ropes and wrought iron nails, are flexible. As usual in timber structures, local joint failures are more likely than a global roof collapse. Embedded timber wall plates run along the lateral walls of the nave and serve partly to support the rafter ends, yet they are discontinuous and are partly non-existent. The structure is built on a base course plinth of rubble stone masonry with mud mortar, over a sloping natural rock, with varying layers of compacted clay.

Due to the sloping ground, the base course rubble stone masonry varies in height typically between 1.2 and 1.5 m, with an extreme value of 3.5 m at the northeast corner. The interior floor level consists of volumes of compacted clay in dry conditions and in the nave is configured

in three elevations, reaching a clear height of 1.6 m in the west part. A significant soil volume forms the floor level in the baptistery and sacristy with heights that reach 3.4 m and 4.0 m respectively. In fact, the base course walls in the baptistery and sacristy act also as retaining walls, counteracting the earth pressures. The lateral walls of the nave have a thickness of 1.6 to 1.9 m and a maximum height of 6.6 m, from ground level. The east and west façade have a thickness of 1.9 m and 1.3 m respectively, and their height, from ground level to the gable ends, is 8.7 m. For the baptistery and sacristy walls, the thickness varies between 0.65 and 2.0 m, with the south wall of the baptistery having a difference in thickness, due to the presence of a choir loft staircase. Buttresses of adobe masonry are placed on either side of the currently infilled openings, although, at the south façade, the buttresses seem to have collapsed. Extensions of walls beyond the corner intersections also serve as buttresses.

Adjacent to the interior face of the east façade there is a choir loft. Wood joists from one side are embedded to the east wall and on the other side they rest on a timber beam. The beam is embedded in the north and south lateral walls and is supported by columns from tree trunks. There is also an exterior balcony, with wood joists cantilevered from the wall of the east facade.

In total five timber ties run along the span of the nave (1 and 3-6 in Figure 3), at the eave level of the lateral walls, placed on top of embedded corbels and in between timber wall plates. Two additional timber ties, in the far west ends of the lateral walls and the timber beam of the choir loft, are also present (7-8 and 2, respectively), as shown in Figure 3. Yet, the whole system is discontinuous and the level of confinement and anchoring is questionable.

The damage configuration, is highly influenced by the low mechanical properties of the adobe masonry, the poor level of confinement of structural parts, and the high level of exposure of the exterior surfaces to erosion, from improper drainage, maintenance and, possibly, condensation. The east façade shows signs of discontinuity with the lateral walls, with evident vertical cracks at both ends, in the entire elevation and thickness. The size and extent of the

cracks are indicative that the east façade behaves largely independently, with out-of-plane critical modes in case of a strong earthquake. Yet, no horizontal cracks at the base are present. The south lateral wall exhibits outward displacements, loss of mortar and units, while the base course has evident signs of erosion and deterioration in many parts of the exterior surfaces, with loose stones and missing mortar from joints.

The baptistery exhibits several vertical cracks, located in the middle span of the sidewalls, which appear to be related to seismic actions or settlements, triggered by the difference in the thickness. The vertical crack at the south corner of the gable wall is characteristic of a separation mechanism of orthogonal walls, from pounding during earthquake events and / or soil settlements [Tolles et al. 1996]. The presence of damage in all the facades is presented in Figure 4 [Zanotti 2015].

3. In situ testing and FE model validation

3.1 Material properties and inelastic behavior

In general, the mechanical properties of adobe masonry have a wide range of variation, depending mostly on the soil characteristics and workmanship. Yet the high level of heterogeneity and large scatter of adobe masonry mechanical properties are evident even on a given site, thus many specimens are often needed for obtaining results of high statistical accuracy. Given also the high level of fragility and limited number of adobe specimens extracted from historic sites, the task of performing advanced testing on adobe masonry is difficult [Angelillo et al. 2014]. Since there were no adobe wallets specimens tested from the Kuño Tambo Church, the average compressive strength of 0.45 MPa was accounted from compression tests on adobe wallets, taken from case study buildings in the center of Lima and Ica ["SRP" 2014].

The modulus of elasticity E of masonry is usually considered associated with the compressive strength f_c by $E_m=a \cdot f_c$, with a wide range of variation in a, which according to Tomazevic 1999 is from 200 to 1000, whereas in "FEMA 306" 1998, the recommended relationship for existing masonry is $E_m=550 \cdot f_c$. A value of a closer to the lower bound specified by Tomazevic 1999 is chosen, which corresponds to a Young's Modulus for the adobe masonry of 100 MPa [Angelillo et al. 2014]. The cohesion c is equal to 0.0445 MPa and the internal friction angle θ is equal to 31 degrees, from adobe triplets ["SRP" 2014, Grau et al. 2006, Lumantarna et al. 2014]. The tensile strength is assumed equal to 0.05 MPa ["EN 1996-1-1" 2005, "FEMA 356" 2000]. Regarding the rubble stone base course, the mechanical properties were specified from ["OPCM 3431" 2005].

Solid masonry parts were modelled as an equivalent homogeneous isotropic material. This approach is found suitable for large structural entities [Lourenço 1996]. The concept of modelling masonry as an orthotropic material is of inherent complexity, and is incorporated through yield surface models, with different yield values along the material axes. However, the process leads to computational difficulties and requires the definition of many inelastic parameters, defined by additional tests [Lourenço 1996]. Here, it is noted that there is a significant uncertainty in applying advanced models to monumental buildings (material properties, construction phases, existing damage and many others), with structural elements made with multi-leaf walls, multiple layers of materials in vaults and irregular masonry unit arrangement. In case of adobe masonry, usually the masonry units and mortar joints are made of the same material, and cracks do not follow the unit arrangement. Therefore, an isotropic material model seems to be the most adequate and validated for adobe masonry e.g. in Pereira et al. 2016 , Tarque et al. 2014, and for monumental buildings in Varum et al. 2014, Ciocci et al. 2017 and Asteris et al. 2014. Notably, studies of combined responses, from dynamic

nonlinear analyses and shaking table tests in masonry buildings, showed good agreement and correlation, in terms of collapse mechanisms and crack formation, e.g. [Mendes 2012].

The physical nonlinear compressive and tensile behavior is defined through a total strain rotating crack model, of inelastic mechanisms evolving from the state of diffused micro-cracks to localized macro-cracks. This quasi-brittle behavior, representative of cementitious materials, can also describe accurately the softening and cracking phase in masonry. Cracks are quantified by the integral of the stress-displacement diagram, denoted as fracture energy G_f^I for tension and G_c for compression [Lourenço 1996]. A default value for the crack bandwidth is assigned, equal to $\sqrt[3]{V}$, where V is the volume of the solid element ["DIANA" 2014]. Tensile stresses are assumed to diminish exponentially, while compression combines a hardening and a softening parabolic phase. It is noted that the adoption of this approach for adobe masonry, and for the element size used, provides for cracking and equivalent linear ultimate cracking strain that ranges between 2 and 6 times the elastic peak strain. This is intrinsic to the modeling strategy and replicates the expected quasi-brittle behavior.

During the experimental in situ campaign, direct and indirect sonic tests were conducted, regarding one indirect setup in the rubble stone masonry, and two indirect and one direct setups for the adobe masonry, in specified locations, as shown in Figure 5 [Greco et al. 2015]. The results of the sonic tests, in terms of Young's Modulus, for the adobe masonry exhibit low values of coefficient of variation, whereas the values for the stone masonry are more disperse, mainly due to the irregular bond. Given the high variability on material properties and unavoidable restrictions on the testing implementation campaign two sets of values were adopted, accounting for upper and lower bounds in stiffness, one with low values of Young's Modulus, from literature, and one with higher values, from sonic tests. The above process was found appropriate, expressed later in terms of lateral resistance values. The adopted mechanical properties, and the recommended fracture energy values [Lourenço 2014], for the adobe and

rubble stone masonry are presented in Table 1. For simplicity purposes, the more conservative model, with material properties from literature is denoted as Global Model 1 (GM1) and the one with material properties retrieved from the in situ sonic tests is Global Model 2 (GM2).

The elastic mechanical properties of timber ties, wall plates and lintels are determined from characterization tests in two case study buildings ["SRP" 2014], with the highest values assigned to the timber lintels (Table 2).

3.2 Dynamic identification tests

Given the unavoidable restrictions and limitations on testing implementation campaigns and the high level of structural diversity in terms of damage and soil-structure interaction, dynamic tests can provide a good contribution on determining the actual structural behavior and damage state of historic structures [Ramos 2007]. In particular, dynamic identification tests can be used as an effective qualitative indicator on the level of separation between walls and the contribution of the system of timber ties, under lateral loading.

The dynamic behavior of the church of Kuño Tambo was identified from ambient tests carried out in May 2015, in order to determine the natural frequencies, the mode shapes and the damping ratios of the structure [Greco et al. 2015]. For the tests, piezoelectric accelerometers were used with a frequency range of 0.15 to 1000 Hz, measurement range ± 0.5 g and a sensitivity of 10 V/g. The signals were recorded by an acquisition system of 24-bit resolution, with frequency sampling equal to 200 Hz, duration equal of approximately 40 min and were processed by ARTeMIS software (SVS, 2006), in which the Stochastic Subspace Identification Method (SSI), namely the Unweighted Principal Components (UPC) Method and the Enhanced Frequency Decomposition Domain Method (EFDD) were used. In total four setups were carried out, with one reference accelerometer and three accelerometers in each setup. The chosen monitoring points were in the top parts of the lateral walls of the nave, in the gable ends of the

east and west façade, as well as in the gable wall of the baptistery and are depicted in Figure 6. It is noted that the reference accelerometer, located close to the middle span of the south lateral wall, was chosen under preliminary modal analyses, revealing the highest amplitude.

Instead of clear transversal and longitudinal modes with integral structural behavior, each wall is excited independently, with out-of-plane bending modes, in single and second order curvatures, similar to those of a cantilevered beam, as shown in Figure 7. These configurations provide feedback on the absence of box behavior, the low level of connectivity at the corners and the obvious deactivation of the ties. Also the walls are excited under the same (or similar) frequency, with high peaks and similar amplitudes, due to similar stiffness, mass and damping properties.

The 1st mode (1.59 Hz) corresponds to the dominant mode in the transversal direction of the nave. Both the lateral and gable walls of the nave experience a symmetric 1st order out-of-phase excitation with high peaks. In the 2nd mode (2.15 Hz) the configuration is similar, except that the south wall of the nave has a 2nd order curvature, with a deflection point near the middle span. The 3rd mode (2.68 Hz) corresponds to a complex mode, which involves the in-phase and out-of-plane excitation of the lateral walls, with the west façade in a 2nd order curvature.

3.3 FE model generation

A 3D FE model was built in Midas FX+ Version 3.3.0 for DIANA software, according to the generated 3D CAD model. The model, as seen in Figure 8a includes the nave, with the adjoining buttresses, the sacristy and baptistery, the corresponding base course foundation, with the differences in elevation, and the system of timber ties and anchors. The base connection was modelled as fixed, while all intersecting adobe walls and the connection between the plinth and adobe were modelled with full connectivity. Given the low tensile strength of the materials, cracks can easily arise upon increasing loading.

According to one visible connection on the southeast corner (see Figure 8b), the configuration of the anchoring consists of a combination of three to four single tie beams of 0.6 m length, fixed in the exterior top surface of the lateral walls and in the level of the choir loft. The tie trusses, of 20 cm in diameter, are not bonded along their embedment in the adobe walls.

The created FE mesh is composed of 321 827 isoparametric tetrahedral linear elements, two-node truss elements, representing the tie beams, 3D two-nodded beam elements, for the anchor beams ["DIANA" 2014]. The size of the tetrahedral elements is 30 cm, while a more refined mesh, of element size of 15 cm, was adopted for the east arched opening. Thus, in the thickness of the structural elements, seven elements per thickness are present in the lateral walls of the nave, while four and six are present through the thickness in the west and east façade respectively.

The roof is not a part of the global FE model, due to the absence of functional rigid formed trusses. The resulting lateral thrust is taken by the lateral walls and is assigned as a uniform distributed load, on the top surface of the adobe walls and gable ends, with a vertical and horizontal component. The total vertical and lateral load of the nave roof was calculated as 326 kN and 165 kN respectively.

Regarding the base course walls in the baptistery, sacristy and nave, they also act as retaining walls, counteracting the earth pressures, from the backfill soil that forms the floor. The backfill soil was modelled as distributed surface load, in three zones, approximating the triangular distribution of the Coulomb earth pressure [Bowles 1977]. The consideration of a dry compacted clay backfill was adopted, by assuming an adequate level of drainage and permeability of the backfill materials [Bowles 1977].

For a smooth vertical retaining wall, with a horizontal backfill, the pressure is calculated from Equation 1, where K_a is the horizontal active earth pressure, φ is the friction angle of the

soil, taken as 20° [Bowles 1977], H is the depth coefficient and the specific gravity of the backfill soil γ, with an assigned value of 26.5 kN/m^3 [Bowles 1977].

$$P_a = \frac{1}{2} K_a \hat{\gamma} H^2 \ \ , K_a = \frac{1 - sin\,\varphi}{1 + sin\,\varphi} \qquad \text{Equation 1}$$

Regarding the openings, timber elements were assigned in the spans. Limited information regarding their geometry and mechanical properties is available, but visual inspection indicates that no damage is present. Square linear elastic timber lintels of 30 cm thickness were chosen for the large openings, with a bearing length of 50 cm, while for the small ones, a size of 25 cm and a load bearing length of 20 cm were considered (Figure 8c and d).

3.4 Structural damage validation though dynamic properties at current state

In a preliminary modal analysis investigation, the mode shapes, for both sets of material properties, were obtained (Figure 9a and c). The structure experiences local modes with corresponding low values of mass participation. The total cumulative percentage of mass participation is reaching 90% only for frequencies around 40 Hz. Mode 1, with a frequency of 2.48 Hz and 4.11 Hz, for model $GM1_{\text{with-ties}}$ and model $GM2_{\text{with-ties}}$ (see section 3.1) respectively, is considered the 1st transversal mode, involving mainly the out-of-plane movement of the lateral nave walls, in a symmetric in-phase pattern. Due to the higher values of Young's Modulus in model $GM2_{\text{with-ties}}$, the structure is stiffer and is excited in higher resonant frequencies. Otherwise, with no tie beams considered, the 1st plane mode only excites the south lateral wall at a frequency of 1.75 Hz and 3.02 Hz for models $GM1_{\text{no-ties}}$ and $GM2_{\text{no-ties}}$ respectively (Figure 9b and d). The presence of ties clearly affects the global mode shapes of the nave in the transversal direction, as it provides confinement and lateral restraint.

From the results of the dynamic identification in situ tests, an evident decrease of the natural frequencies and an alteration of the mode shape vectors are found, in comparison to the

results of the modal analyses, with total continuity in the wall connections, and no ties present. Dynamic model validation and fitting can provide substantial information on the current level of damage and discontinuity between parts [Ramos 2007]. Therefore, a calibration of the numerical model of the church was conducted, updating the soil stiffness, the level of connectivity of intersecting walls, and the localization of damage, introduced as vertical cracks. The fitting process of the experimental data, for both models $GM1_{no\text{-}ties}$ and $GM2_{no\text{-}ties}$, was conducted by adjusting the frequency of the 1st mode and the mode shape vectors, changing the stiffness at the base and at the intersection planes between walls (replicating existing cracks).

The deformation of the foundation seems a realistic scenario, considering the high rate of deterioration, in adobe and base course masonry parts, and the presence of the compacted layer of clay, between the base course foundation and the bedrock, documented through in situ inspections. Clay being very susceptible to saturation and volume fluctuations, upon wetting and drying, can fluctuate in volume and during desiccation, differential settlements are bound to occur [Bowles 1977]. Furthermore, clay is characterized by relatively low frictional strength, with friction coefficients of 0.165 at lower bound, depending on the percentage of clay [Tembe et al. 2010]. In order to account for the soil-structure interaction, translational springs in three directions were added to the model. The stiffness of the springs was considered as a variable, with the tangential stiffness being equal to 40% of the normal stiffness [Lourenço 1996].

For the modelling of existing cracks, interface elements were used, in order to simulate the weak orthogonal connections between walls, the vertical cracking in the sidewalls of the baptistery and the discontinuity in the buttresses (Figure 10). These are modelled as two surfaces of three-nodded linear isoparametric interface plane elements, extended until the base of the walls. For a modal analysis, linear elastic interface elements are sufficient, with focus on crack opening. Thus, the interface planes are characterized by very low stiffness, with updated parameters in the range of 10^{-4} to 10^{-3} N/mm^3. This indicates real cracks, as normal stiffness

values for masonry are in the range of 10 to 100 N/mm^3 [Lourenço 1996]. If nonlinear static analyses were to be performed, replicating current conditions, nonlinear stiffness elements need to be used, with very low stiffness in tension and shear, while the stiffness in compression should be higher after a closing crack gap value. A combined cracking-shearing-crushing interface material model, simulating tensile, compressive and shear fracture softening, would be appropriate [Lourenço 1996]. It is stressed that the adopted model finally in this paper, for the structural analyses, has no damage included, as the objectives are to verify if the existing damage can be replicated by the model under earthquake loading and what would be the safety of the structure if the same would be repaired but not strengthened.

The first tuning involved the stiffness of the 3D foundation springs, in order to shift the frequency of the 1st mode of the models to the experimental frequency of the 1st mode shape (1.59 Hz). Later on, the stiffness of the vertical interface elements was adjusted in order to match the mode shape vectors in each wall of the nave. Table 3 summarizes the elastic updated parameters of the interfaces and the foundation springs, whereas the mode shape configuration of the first three modes of the updated models, in comparison with the ones of the dynamic tests, is depicted in Figure 11.

The numerical correlation between two sets of mode shape vectors was done with the Modal Assurance Criteria (MAC), given by Equation 2 [Mendes 2012], where φ^u and φ^d are the normalized mode shape vectors of two different modal conditions and n are the degrees of freedom, which in this case are the positions of the accelerometers and the corresponding nodes of the numerical models. MAC values varying from 0 to 1, imply uncorrelated (orthogonal) vectors and perfect matching between the two mode shapes respectively. The model GM2$_{\text{no-ties}}$ presents the highest MAC value of 0.83 in mode 1, which denotes a sufficient correlation. The corresponding MAC value for model GM1$_{\text{no-ties}}$ is 0.44. For higher modes the correlation is low, despite the close frequencies and similar mode shapes.

$$\mathrm{MAC}_{u,d} = \frac{\left|\sum_{i=1}^{n} \varphi_i^u \varphi_i^d\right|^2}{\sum_{i=1}^{n} (\varphi_i^u)^2 \sum_{i=1}^{n} \left(\varphi_i^d\right)^2} \qquad \text{Equation 2}$$

4. Safety of the structure in original configuration

The main objectives of the conducted numerical analyses were to evaluate the structure's capacity of sustaining its own weight and the lateral capacity under seismic loading, for the current configuration, but undamaged. Therefore, the existing cracks and interfaces are not included in the initial structural model. Given the fact that two sets of material properties were defined, regarding the Young's Modulus, results from both models GM1 and GM2, will be presented. Thus, high variability, in material properties, would be expressed in terms of upper and lower bounds of lateral resistance values, accounting for safety. Correlation with the existing damage pattern upon loading provides a basis for the actual causes of structural damage. Verification of the lateral capacity at the weakest directions was provided by kinematic analyses for the damage (DLS) and ultimate limit state (ULS).

4.1 Nonlinear static analysis

4.1.1 Gravity loading

The global structure, with no ties present, was first subjected to increasing dead load up to full gravity, including the thrust from the roof and the passive earth pressure from the elevated floor. Here, it is noted that the lateral thrust can be partly reduced in the presence of lateral wall displacements.

The south unrestrained lateral wall is bending outwards due to the lateral thrust from the roof, while the outward top displacement of the north lateral wall is smaller, due to the presence of buttresses and orthogonal walls of the baptistery and sacristy. All displacements are in the order of millimeters, with the maximum displacement, recorded at the top eave of the south

lateral wall, being equal to 10.6 mm and 3.6 mm, for Models $GM1_{no\text{-}ties}$ and $GM2_{no\text{-}ties}$ respectively. The level of vertical compressive stresses at the foundation base are in the range of 0.1-0.3 MPa, which is rather moderate.

The tensile damage of adobe masonry parts for both cases, is concentrated in small areas at the top corners of the nave, around some timber lintels and in a small interior area in the stone masonry of the sacristy. Most of the damage is related to lateral forces (roof load and earth pressure), yet the level of tensile strains is quite low, with respect to the cracking strains, and the damage area is very small. This damage would not be visible, given the small crack width, and is, thus, of minor importance. Therefore, it can be concluded that both models behave almost elastically under gravity loading.

With the presence of ties, the transversal displacements are lower in models $GM1_{with\text{-}ties}$ and $GM2_{with\text{-}ties}$ by three and two times respectively, given the larger stiffness of the north part of the structure and the joint global behavior. The ties are activated with moderate tensile stresses, with the maximum axial stress found in the ties close to the middle span of the nave, equal to 0.8 MPa.

4.1.2 Pushover analysis

Regarding the seismic effects, lateral loading was applied using a mass proportional approach in all primary directions, until the structure enters post-peak behavior and collapses, thus assessing safety levels and obtaining failure mechanisms. The convergence criterion for each equilibrium state is based on the internal energy, with a convergence criterion of 10^{-3}. Through the first steps, a standard Newton-Raphson iterative method was used. Subsequently, close to peak, the Arc Length Control method, in a spherical path, was used. Displacement constrains were typically gathered from all nodes, so as to control global collapse mechanisms. Yet, given the local failures, in a later failure sequence, only specific control points were considered, on the elements of interest [‘DIANA’ 2014].

The tying system was proven to be ineffective, without offering any significant lateral restrain or uniform transversal behavior. Thus, numerical results are discussed for models GM1 and GM2 without ties present, in terms of load capacity curves and principal crack width plots, with iso surfaces of structural cracks in red (1-3mm).

In existing masonry structures, critical out-of-plane resistance occurs under the rigid body motion of individual parts [Lourenço et al. 2011, 'FEMA 356' 2000, Varum et al. 2014]. At the level of the rotation plane, compressive behavior can be relevant for assessing safety under seismic loading [Tomazevic 1999]. Due to the high inertia forces, failure zones close to the intrados of the rotation plane are under toe crushing. With the increase in lateral deformation, crushing zones gradually progress along the thickness of the walls, influencing the stability and overall post-peak behavior of the upper structure. Still, in most cases, the maximum force capacity is weakly affected by the compression toe. In the present case, even if the material is rather weak in compression, the very large thickness of the walls and the low height of the structure, confirm the moderate influence of the compression toe failure. Crushing, under compressive stresses, is monitored through minimum principal strain plots, with gradients reaching ultimate strain values, in blue.

Due to the uncertainty in the material properties, the minimum lateral capacity values in all primary directions define acceptable, stringent bounds for the seismic vulnerability of the structure without damage; i.e. Model $GM1_{no\text{-}ties}$. Nevertheless, differences in lateral capacity between both models are about 20% and are considered moderate.

The results from the pushover analyses in the positive x-x direction (see Figure 8 for the model axes), for Models $GM1_{no\text{-}ties}$ and $GM2_{no\text{-}ties}$, are presented and superposed in Figure 12a. Model $GM1_{no\text{-}ties}$ exhibits the minimum lateral capacity of 0.22g, while Model $GM2_{no\text{-}ties}$ is stiffer and the lateral capacity is around 30% higher. By comparing the failure modes for Model $GM1_{no\text{-}ties}$, at a load step near collapse, with a maximum total displacement of about 25 cm, the

damage is more concentrated on the west part (Figure 12a). The failure mechanism consists of vertical separation cracks, along the corners, in the west part of the church, covering the entire elevation and thickness, with horizontal hinge lines at the bottom of the base course foundation, which results in the collapse of the west gable and side walls. As the tensile damage propagates along the entire thickness of the walls, the west part becomes structurally independent.

When the lateral load is applied in the negative x-x direction, the failure mode consists mainly of the out-of-plane overturning of the east façade, together with adjacent fragmented front parts of the lateral walls, as shown in Figure 12b. The minimum obtained lateral capacity is 0.28g ($GM1_{\text{no ties}}$), with the first tensile damage (cracks ≥ 1mm) initiating at 0.10g at both corners of the east façade, organized in a vertical fragmentation and increasing in thickness. At 0.27g the vertical separation of the east façade is completed, while vertical cracks appear at the middle span of the east side wall of the baptistery and at both the gable walls of the baptistery and sacristy. Also horizontal hinge lines initiate at the adobe-stone masonry interface of the east façade. The respective load step for the stiffer model ($GM2_{\text{no-ties}}$) corresponds to 0.34g.

The resulting tensile damage seems to efficiently reproduce the existing damage pattern in the east façade and the gable wall of the baptistery, as shown in Figure 12b of ($GM1_{\text{no-ties}}$), with crack widths up to 8 cm. Due to the varying stiffness caused by the staircase void in the east baptistery wall, tensile damage is initiated near the middle span, which can be correlated with the documented vertical crack at the same place (Figure 14). In particular, the initiation of vertical cracks in the side walls of the baptistery appears to be triggered by seismic loads, but according to the in situ observation, the vertical cracks fully propagated in elevation. Thus, the documented damage appears to be the result of seismic action and settlements.

For the pushover nonlinear analysis along the positive direction of the y-y axis, the failure mechanism consists of the separation and out-of-plane overturning of the south lateral wall, with large deformations. The structure's lateral capacity reaches 0.19g and 0.22g, for Models

$GM1_{no\text{-}ties}$ and $GM2_{no\text{-}ties}$ respectively, with maximum outward displacements recorded at the middle top of the south lateral wall (Figure 12c).

As shown from the distribution of the principal crack widths in Figure 12c, in load steps of corresponding lateral displacements of about 0.25 m, the south lateral wall follows an out-of-plane collapse mode, with significant tensile failure zones at the intersections with the west and east façade. Under the formation of a continuous flexural crack, at the interface with the base course foundation and at base, a rigid out-of-plane body motion is defined. Following the lateral loading in progress, in Model $GM1_{no\text{-}ties}$, the first tensile damage (cracks ≥ 1mm) initiates at 0.05g, at the top of the southeast corner, propagating diagonally at the thickness of the connection. At 0.11g, cracking at the southwest corner appears, and at 0.17g, the horizontal flexural crack at the base of the foundation base initiates. Next, propagation of the horizontal hinge line follows the adobe-stone masonry interface and is associated directly with the vertical fragmentations at both corners, forming the collapse mode of the south lateral wall. The large peak, in terms of incremental displacements, occurs during the post-peak behavior, at a lateral displacement of about 14 cm. In the following steps, the south lateral wall is in rigid body motion with large incremental displacements. The stiffer model ($GM2_{no\text{-}ties}$) exhibits a similar collapse mechanism. Due to the higher Young's Modulus in adobe and rubble stone masonry the structure enters the plastic range and sustains a moderate damage level with higher residual capacity.

The results from the pushover analysis in the negative direction of the y-y axis are presented (Figure 12d). The lateral capacity is controlled by the early failure of the sacristy gable wall and in this case is 0.16g and 0.25g, for Models $GM1_{no\text{-}ties}$ and $GM2_{no\text{-}ties}$ respectively. The capacity of the south lateral wall is much larger than in the positive y-y axis, due to the external lateral parts and buttresses contributing much more to the overall stiffness of the nave. In both models, the sacristy is severely damaged, with vertical tensile failure zones in the

corners of the side and gable walls, as seen from the ultimate principal crack width distribution, with a displacement of about 26 cm (Figure 12d). Yet, no such damage exists on current state. Specifically, the structure in model $GM1_{no\text{-}ties}$ enters a rigid body motion mechanism at 0.08g, while the horizontal hinge line at the base of the south lateral wall is formed, when the local lateral capacity reaches 0.36g. In model $GM2_{no\text{-}ties}$, the south lateral wall behaves as a structural mechanism at 0.39g and a corresponding horizontal displacement of about 5 cm.

Lastly, from the nonlinear pushover analyses, in all principal directions, the rotation plane is formed mainly at the lower level of the rubble stone base course. Crushing zones, in corner junctions and at the rotation plane, appear to follow the same paths with tensile failure, accounting for the combined effect of localized out-of-plane bending. Yet, in open cracks, of pure tensile failure, compressive failure appears due to the Poisson effect and should be ignored as unrealistic. In areas of pure compression; i.e. rotation planes, toe crushing appears in late steps of the post peak, at corresponding lateral displacements values within the range of 10 to 16 cm, so not much influencing the maximum load capacity (Figure 13). In fact, no compressive failure is documented, when the structure enters the post-peak, as shown in Figure 13. This seems reasonable given the very large width of the walls and low height of the building (the vertical stress under self-weight is extremely small). At ultimate lateral displacements of around 30 cm, crushing zones cover half the thickness in specific locations, but at this stage the model is hardly representative of reality. In model $GM2_{no\text{-}ties}$, horizontal crushing zones appear less intense and initiate at similar lateral displacements, compared to model $GM1_{no\text{-}ties}$.

4.2 Nonlinear dynamic analysis

A nonlinear dynamic analysis with time integration was also conducted. Here, the objective was to discuss the dynamic global response to an earthquake ground motion input and to compare damage patterns and collapse mechanisms, with the results of the pushover

analyses, under lateral loading. The expected tensile damage in masonry buildings, of low tensile strength, under earthquake excitation, is more distributed, with cracks closing, reopening and propagating [Mendes 2012]. Global response outputs are mainly in terms of superposed maximum principal tensile strain scans, vectorial diagrams in elevation, relative displacement-time history plots and hysteretic curves [Lourenço 2002].

In general, for large numerical models, nonlinear dynamic analysis with time integration is a complex and time consuming process and requires vast computational capabilities. Yet, is the most accurate approach, representative of a global structural response, under earthquake excitations. Given the recommendations provided by Eurocode 8, at least seven time-history analyses need to be performed, with uncorrelated accelerograms, and mean output values are to be considered. Alternatively, if less analyses are performed, one can consider the maximum output values ["EN 1998-1" 2004].

The obtained results depend on the representation of the actual geometry, the type of hysteretic behavior, the adopted constitutive material models, the global damping characteristics, and the nature and characteristics of the applied accelerograms (artificial or natural), among other features. Artificial accelerograms are generated from the considered elastic response spectrum, whereas natural accelerograms are obtained through recorded earthquake histories, which are later scaled and matched, according to the required PGA and elastic response spectrum. Yet, the option of scaling those recordings under high differences of magnitude will result to high differences in the frequency content and the signals will not be representative of an earthquake of high intensity [Stewart et al. 2001]. The actual frequency content of a real ground motion is dependent on parameters of high variability; i.e. the local geology, the type of earthquake. A selection of a single natural earthquake event can often be unsatisfactory, since it contains unique random parameters, which will not occur again [Mendes 2012]. On the other hand, generated accelerograms from design response spectrums and a

desired amplitude, acknowledge a wide range of regional seismic risk and a widely distributed energy content, within a broadband range of frequencies [Trovato et al. 2017], so they were used here. Also the type of integration method and the selected time step are of importance [Lourenço 2002, Mendes 2012].

The same material properties and inelastic behavior were adopted, as for the nonlinear pushover analyses, under equivalent seismic loads (see section 4.1). The chosen model was $GM2_{no\text{-}ties}$. With material properties validated through in situ sonic, this model appears to be the best representation of the structure.

A series of eight uncorrelated artificial accelerograms, with a duration of 25 sec and increments of 0.01 sec, were generated by means of LNEC-SPA software, from which two, with the best fit were chosen to be applied as base excitation in the principal horizontal directions of the structure (North - South, East - West), as shown in Figure 15a [Mendes 2008]. The selected response spectrum of the accelerograms is compatible to the type 1 (high intensity earthquakes of M_S>5.5) design response spectrum, defined by Eurocode 8, a damping ratio of 5% and a type A for the soil (rock, S=1) ["EN 1998-1" 2004]. The target PGA is 0.30g, according to the seismic demand for the Cusco region, when the analysis was conducted ["NTE-0.30" 2003], as shown in Figure 15b. Baseline correction filters were applied in all signals, by using a bandwidth Fourier filter with a frequency range from 0.5 to 100 Hz, in order to eliminate background noise and to set starting and ending point displacements to zero.

In dynamically induced phenomena, the response of a building in terms of dissipated energy is a composition of inelastic behavior and viscous damping [Chopra 2001]. It is noted that secant unloading-reloading has been used in model, being this representative of cracking failure. Compressive damage is not much relevant around peak and will not much influence the response at this stage, as stated before. Here, Raleigh viscous damping $\underline{C}$ matrix is considered, under a linear relation of mass $\underline{M}$and stiffness $\underline{K}$ matrices:

$$\underline{C} = a\underline{M} + \beta\underline{K} \qquad \text{Equation 3}$$

where α and β are weight coefficients, in relation with the damping ratios ξ_i and one set of natural frequencies ω_i, usually considered as the frequency of the fundamental mode ω_1 and the frequency of the higher mode of interest ω_2 [Chopra 2001].

$$\xi_i = \frac{1}{2}\left(\beta\omega_i + \frac{\alpha}{\omega_i}\right) \qquad \text{Equation 4}$$

Here, for a damping ratio of 3%, acceptable for masonry structures according to [Chopra 2001] and an upper bound frequency bandwidth, corresponding to 70% of cumulative participation mass, the weight coefficient constants α and β are set to 1.01024 and 0.00036 respectively. In between the modes of interest and as the damage will propagate during the nonlinear dynamic analysis with time integration, values of frequencies and damping ratios will change, according to the abovementioned equation, as shown in Figure 15c.

The quasi-brittle failure in masonry structures, under dynamic excitations, introduces limitations in accuracy, with conditionally stable time step dependent solvers. Due to the transition from the linear state to the fully cracked one, with a drop to almost zero stiffness in these locations, numerical noise initiates, in forms of high frequency spurious vibrations [Hilber et al. 1977, Mendes 2012]. Thus, the Hilber-Hughes-Taylor (HHT) time integration method (the α method) is used. The HHT method is an extended version of the Newmark method, unconditionally stable, which introduces numerical damping properties with increased accuracy, in structural dynamic problems of direct time integration. Similarly to the Newmark method, the HHT method is an implicit numerical integration process [Hilber et al. 1977, Mendes 2012].

An important parameter in the nonlinear time-history analysis is the definition of the time step interval Δt. According to [Mendes 2012], the assigned time step intervals should be of size sufficiently small, compared to the total duration of the analysis. In order to account for the mode contribution of the highest frequency f_i, with an error lower to 5%, the time step should

follow Equation 5. Here, a time step interval of 0.004 s was chosen, corresponding to 6250 steps.

$$\Delta t = \frac{1}{20} T_i \qquad \text{Equation 5}$$

The results of the nonlinear time history analysis are qualitative, e.g. in terms of induced tensile damage, and can be correlated with in situ documented damage patterns. Yet, given the randomness and amplitude variation of past earthquake excitations, if any in a given location, the obtained damage patterns can differ in intensity and distribution from the documented ones. Also non-incorporated parameters, such as alterations, reconstructions, additional embedded elements and the approximation level of the actual material characterization can alter and increase the scatter of response. The induced damage, was shown by superposing all extreme maximum principal strains, along the duration of the ground motion, in one plot; i.e. a maximum principal strain scanning plot. The compilation of the extreme values of tensile damage, in time, can reproduce the entire damage pattern, which is well correlated with the damage in situ (Figure 16a). Vertical fragmentations in the corners of the south façade, together with vertical and diagonal shear cracks in the front part of the lateral nave walls, the side and gable walls of the sacristy, are well defined and consistent with the current damage (see Figure 4). In the south lateral wall, along with the clear out-of-plane failure mechanism, the tensile cracks have a wider dispersion in a diagonal pattern, indicative of out-of-plane bending failure, with consistency to the present damage on top of the infilled side gate and in the proximity of the interior pilaster. Comparing with the results from the pushover analyses, the failure modes in all principal directions are identical (see Figure 16a and b). Yet, the tensile damage distribution, due to the static out-of-plane loading application, is localized in a few zones, rather than distributed in the entire envelope, as in the response under earthquake excitations.

A comparison, in terms of maximum capacity values and out-of-plane displacements, with the results of the nonlinear pushover analyses is challenging. The relative displacement-

time history plots, in the same monitoring points, as in the capacity plots of the nonlinear pushover analyses, are shown in Figure 17. Here, in all graphs, positive displacements values refer to external out-of-plane directions. The south lateral wall, presents a maximum out-of-plane displacement of around 8 cm, while for the east and west gable walls is less. The cyclic displacement oscillation around zero is under lower frequencies than of the east and west gable walls, which clearly denotes an asymmetric response, with the more ductile behavior and low stiffness in the north-south direction. Here, it is noted that the displacements under earthquake excitation, are not absolute values and cannot be directly compared with results from pushover analyses, since the configuration of the dynamic failure mode is not always clear and there is a higher diffusion of tensile cracking. Yet, none of the structural elements of the nave present residual displacement amplifications, indicating that collapse was probably not found. On the contrary, the displacement-time history plot of the sacristy's gable wall is under increasing residual amplification, denoting that a rigid body motion is evolving exponentially and a clear out-of-plane collapse has occurred in the last steps (see Figure 17c), also confirmed from pushover analyses. No such damage is present in situ, but there is also no historic record of such a local destructive earthquake in the past.

The ductility of the structure, including dissipation capacity, plays a major role in the response of seismic actions. Base shear load factors-time histories in both principal directions (see Figure 18a and b) are indicative of the seismic capacity under dynamic loading and are generally of lower amplitude than the input acceleration signals. Figure 18c to f depicts hysteresis curves (relative displacements vs base shear) in all four principal directions, superimposed with the load displacement curves from the pushover analyses. The displacement envelope of the south lateral wall is wider towards out-of-plane direction (positive x-x axis), as expected, due to lack of restraint, with a maximum seismic coefficient of 0.26g. Towards the end of the excitation, at a lateral displacement of 6 cm, the wall is under post-peak softening

control, with an evident decreasing slope. The sacristy's gable wall (see Figure 18d) is under increasing residual top displacement amplitudes and at around 25 cm the lateral capacity is lost, which constitutes out-of-plane overturning. As for the west and east gable walls (see Figure 18e and f), during the entire duration of the seismic event, they maintain a high rate of dissipating energy, with well-defined load cycles and no drops in base shear reactions. From the comparison with the pushover curves, it is clear that both gable walls behave still elastically and for obtaining the maximum seismic coefficients and collapse modes, the structure needs to be subjected to an earthquake of higher intensity.

4.3 Seismic demand and displacement control

4.3.1 Kinematic analysis

Given the low level of connectivity between adjacent structural parts, in adobe masonry envelopes, without box behavior, seismic failure mechanisms can be studied through more simplified analytical models, which can correlate well, even with complex numerical modelling [Lourenço 2002]. Limit analysis offers an insight on structural load at failure by following a kinematic approach and specifying out-of-plane mechanisms. Here, the specific failure mechanisms were verified, according to the results of the numerical analysis, based on Italian standards ["OPCM 3431" 2005, "NTC" 2008]. In particular, through a simplified linear kinematic approach, lateral forces and displacements were checked for the damage (DLS) and ultimate limit state (ULS). The ultimate limit state (ULS) will determine the safety margin with respect to collapse. Two different methods will be accounted for; a linear kinematic analysis with the use of the behavior factor q, related to the ductility, and a nonlinear kinematic analysis through the capacity spectrum.

4.3.1.1 Hypotheses

For the application of the limit analysis, the following hypotheses are considered [Franchetti 2014]:

1) Zero tensile strength of masonry;
2) Unlimited friction between blocks;
3) The compressive strength is accounted in order to place the rotating hinge line inside the thickness of the elements. According to the Italian code and a triangular distribution of the compressive stresses at the base, the position of the hinge t is given by Equation 6, where $\Sigma_i W$ is the resultant of the vertical forces, σ_r is the compressive strength of the material and l is the transversal length of the effective area. Alternatively, a uniform stress distribution with an effective compressive strength, equal to 80% of σ_r, can be adopted, which seems more appropriate for the ULS. The corresponding plastic hinge position is given by Equation 7 (Figure 19), which is similar to the triangular distribution, in case of a rectangular cross section but, conceptually, more appealing and is much easier to apply in non-rectangular cross sections.

$$t = \frac{2 \cdot \sum_i W_i}{3 \cdot \sigma_r \cdot l} \qquad \text{Equation 6}$$

$$t = \frac{\sum_i W_i}{2 \cdot 0.8 \cdot \sigma_r \cdot l} \qquad \text{Equation 7}$$

4) The self-weight of the blocks A_i is applied at the center of mass. The action from the roof in the wall is assumed as a uniform line load, in the position of the wall plates, with a vertical and horizontal component F_i, as defined before.
5) The horizontal equivalent seismic forces are proportional to the self-weight loads, with a load multiplier of a_o, applied in the center of mass of the blocks.
6) To account for the ductility of the structure, a behavior factor (q) of two is considered, assuming that the structure is in cracked condition, with a corresponding secant period T_S.

4.3.1.2 Application to south lateral wall

The south lateral wall has a large free span of around 31m and a thickness of around 1.7m. As shown in Figure 20a, the out-of-plane failure covers almost the entire wall, with separation in the corners and a horizontal hinge line, formed, mostly, in the adobe-base course interface. Here, the entire wall is considered for the kinematic mechanism, with a corresponding portion of 1 m length (see Figure 20b). The geometric characteristics of the generic block and the kinematic chain configuration, under a virtual rotation θ_k are shown in Figure 20c. The applied forces and the center of mass (x_{Gi}, y_{Gi}) are given in Table 4.

. The location of the rotating hinge, taking into account a uniform stress distribution from Equation 7 is equal to 0.28m. The vertical and horizontal displacements, correspond to the applied loads, at a given rotation angle θ. Appling the Virtual Work Principle (VWP), the angle θ for which the work of the internal and external forces is equal, provides the solution. The acceleration needed for the activation of the mechanism reads:

$$a_o A_1 \cdot \delta_{xA1} + F_2 \cdot \delta_{xF2} - F_1 \cdot \delta_{yF1} - A_1 \cdot \delta_{xA1} = 0 \Rightarrow a_o = 0.18g$$

In order to obtain the capacity of an equivalent system of one degree of freedom (SDOF), an equivalent value of the acceleration a_o* must be calculated. The transformation provides:

Corresponding equivalent mass: $\mathrm{M}^* = \dfrac{(\sum_i \mathrm{W_i} \cdot \delta_{\mathrm{xi}})^2}{\mathrm{g} \cdot \sum_i \mathrm{W_i} \cdot \delta_{\mathrm{xi}}{}^2} = 19.8 \text{ ton}$

Eccentricity: $e^* = \dfrac{g \cdot M^*}{\sum_i W_i} = 0.96$

$$a_o{}^* = \frac{g \cdot a_o}{e^*} = 0.18 \cdot g$$

For the Damage Limit State verification (DLS), safety is achieved when the acceleration for the activation of the mechanism a_o* is greater than the one specified from the elastic spectrum evaluated for T_o=0 sec (EQ), where a_g is the PGA for the Cusco region, equal to

0.25g, S accounted for the type of soil, which for an intermediate soil is equal to 1.2 ["NTE-0.30" 2016], *Z* is the height the center of mass and *H* is the height of the whole structure.

$$a_o^* = 0.18g \not\geq \frac{a_g \cdot S}{2.5}\left(1 + 1.5\frac{Z}{H}\right) = 0.21g$$

The ULS, with force control can be verified through the equation:

$$\mathrm{a_o^*} = 0.18\mathrm{g} \not\geq \frac{\mathrm{a_g} \cdot \mathrm{S}}{\mathrm{q}}\left(1 + 1.5\frac{\mathrm{Z}}{\mathrm{H}}\right) = 0.22\mathrm{g} \quad ,\mathrm{q} = 2$$

Thus, the unrestrained south lateral wall is not verified for the DLS and the ULS. In an attempt to associate the displacement, from the design spectrum Δ_d and the ultimate displacement capacity of the system d_u*, a displacement control (nonlinear kinematic analysis) is also conducted ["OPCM 3431" 2005, "NTC" 2008]. Here, the Peruvian capacity spectrum is used, with a PGA of 0.25g ["NTE-0.30" 2016].

The required finite rotation θ that zeroes moment M_s is:

$$M_s = \sum_i W_i \cdot R_i \cdot cos(\beta_i + \theta) = 0 \Rightarrow \theta = 11.7^o$$

The maximum corresponding displacement d_o* is:

$$d_o^* = y_G \cdot sin\,\theta \cdot \frac{\sum_i W_i \cdot \delta_{x,i}}{\delta_{x,k} \cdot \sum_i W_i} = 0.68\ m$$

The maximum allowable displacement is defined as:

$$\mathrm{d_u^*} = 0.4 \cdot \mathrm{d_o^*} = 0.27\ \mathrm{m}$$

The corresponding displacement of the SDOF system, with a secant period T_s is:

$$d_s^*(T_S) = 0.4 \cdot d_u^* = 0.11\ m$$

$$a_s^*(T_S) = a_o^* \cdot \left(1 - \frac{d_s^*}{d_o^*}\right) = 0.15g$$

$$T_S = 2\pi \cdot \sqrt{\frac{d_s^*}{a_s^*}} = 1.69\ sec$$

The displacement as derived from the design spectrum of the Peruvian seismic code, at the given period T_s, for seismic Zone 2 (0.25g), a soil factor of 1.2 (intermediate soil), a period T_b of 0.6 s and an assigned behavior factor q of 2, is given by the equation:

$$\Delta_d(T_s) = \left(\frac{T_s}{2\pi}\right)^2 \cdot 2.5 \cdot Z \cdot \frac{S}{q} \cdot \left(\frac{T_b}{T_s}\right) = 0.19\ m \leq d_u^* = 0.27\ m$$

According to limit analysis, the corresponding point of significant structural damage, for a PGA of 0.25g, is 19 cm, but is safe under collapse, with the near collapse limit state starting, for values of lateral displacement, greater than 27 cm, shown in Figure 21.

4.3.2 Pushover analysis

In order to obtain a performance response, under the current seismic criteria set by seismic codes, a displacement based approach was followed, by means of the N2 method in Eurocode 8 ["EN 1998-1" 2004]. The method combines nonlinear pushover analysis curves with an inelastic response spectrum. Thus, the transformation of the pushover curves to those of a SDOF system is needed, in order to perform the comparison. The process is explained extensively in Fajfar 2000.

From the nonlinear static pushover analyses of the church of Kuño Tambo at current state, the propagation of tensile damage and corresponding cracks, eventually separates the structure into smaller structural parts, which can be assumed that behave independently. In the positive y-y direction the controlling failure mechanism involves the larger portion of the south lateral wall, as shown in Figure 22. In a planar section, where the top displacement occurs, the effective quantities, in terms of vertical mass distribution $\boldsymbol{M}$ (diagonal matrix), lateral displacement shape matrix $\boldsymbol{U}$ and lateral force vector $\boldsymbol{P}$, equal to the base reaction vector $\boldsymbol{R}$, are formed in a discretized manner, by dividing the wall in ten horizontal parts of the same height (Figure 22a). Thus the basic equation of motion is formed:

$$M\ddot{U} + R = M1a$$

Here, a is the lateral load vector in units of g and 1 is a unit vector.

The distribution of lateral forces and displacements in elevation is a function of the normalized deformed shape vector Φ of the element in out-of-plane rotation (Equation 8 and Equation 9). In specific, the response is associated to a specified deformed shape or a predominant mode, assumed constant during the evolution of lateral loads, for which the transformation to a SDOF system takes place.

$$U = \Phi D_t \qquad \text{Equation 8}$$

$$P = R = aM\Phi 1 \qquad \text{Equation 9}$$

$\boldsymbol{D_t}$ is the maximum top lateral displacement vector, as a function of load step.

The enforced lateral load distribution is actually set as an initial parameter decision, for the pushover nonlinear analysis of masonry structures and a mass proportional distribution is considered appropriate. When no integral behaviour is present, masonry parts are excited in different frequencies, with varying participation masses, and are subject to failure modes of different type and order. Thus, the choice of a predominant shape mode, is challenging and can be applied solely to individual failing structural parts. In the current case study, the plot of various normalized shapes, during the evolution of the lateral loads, for both models GM1 and GM2 (with no ties present), is presented in Figure 22b. The deformed shape configuration matches the one of the first mode, mostly in the first steps of the pushover analysis, during the elastic range. After the transition to the nonlinear phase, deformed shapes are verging towards the linear distribution (inversed triangle) and a rigid body behaviour. Both extreme deformed shapes will be used for both models GM1 and GM2 and the envelope of the displacement response will be obtained for each case.

The equation of motion for the equivalent SDOF system writes:

$$m^*\ddot{D}^* + F^* = -m^*a$$

The equivalent mass m^*, displacement D^* and force F^* of the SDOF system are given from the equations.

$$m^* = \Phi^T M1 = \sum m_i \Phi_\iota \quad \text{Equation 10}$$

$$D^* = \frac{D_t}{\Gamma} \quad \text{Equation 11}$$

$$F^* = \frac{aM\Phi 1}{\Gamma} \quad \text{Equation 12}$$

The constant Γ, known as participation factor is defined as

$$\Gamma = \frac{\Phi^T M1}{\Phi^T M \Phi}$$

Here, the equivalent mass m^* accounts to 277.13 tons and the participation factor Γ is 1.556.

The pushover curves of the SDOF system, for models GM1 and GM2 are depicted in Figure 23. Next, idealized elasto-perfectly plastic force-displacement curves are obtained by determining the maximum capacity, corresponding to the point of yielding, with F_y and D_y, the force and displacement at yield respectively. The yielding point is associated to the point of the plastic hinge formation, given by Equation 13, which can be determined as point of the slope reversal in the post-peak (Figure 23b). Here, D_m is the corresponding equivalent displacement of the plastic limit and E_m is the dissipating energy. In cases of post-yield hardening, the above limit cannot be determined by the N2 method ["EN 1998-1" 2004].

The expected response to the current response spectrum can be obtained through a graphical process, in a superposed graph, of the elastic response spectrum and the equivalent load-displacement curves of the SDOF systems, as shown in Figure 23a. The point of intersection of the radial line, corresponding to the elastic period T^*, of the SDOF system, given by the Equation 14, provides the displacement response, under the current PGA of 0.25g ["NTE-0.30" 2016]. The displacement envelope for model GM1 is from 10.5 to 10.6 cm and

for model GM2 from 6.1 to 6.3 cm respectively. The differences between the 1st mode and linear based deformed shape hypothesis are considered marginal. The difference in stiffness characteristics, between models GM2 and GM1 (see Table 1) results to an average increase on the displacement response of around 70% respectively.

$$D_y^* = 2\left(D_m^* - \frac{E_m^*}{F_y^*}\right) \quad \text{Equation 13}$$

$$T^* = 2\pi\sqrt{\frac{m^* D_y^*}{F_y^*}} \quad \text{Equation 14}$$

Considering the hysteretic energy dissipation, the inelastic performance can be quantified by the reduction factor R_μ and the ductility performance μ from Equation 15-Equation 17.

$$R_\mu = \frac{S_{ae}}{S_a} \quad \text{Equation 15}$$

$$\mu = \left(1 - R_\mu\right)\frac{T_C}{T^*}\,, T^* < T_C \quad \text{Equation 16}$$

$$\mu = R_\mu\,, T^* \geq T_C \quad \text{Equation 17}$$

Here, S_a and S_{ae} are the inelastic and elastic acceleration of the SDOF system and T_c is the spectral period that defines the transition limit from the constant acceleration to the constant velocity branch. For the Peruvian elastic response spectrum and an intermediate type of soil, T_c is equal to 0.6 s ["NTE-0.30" 2016]. For models GM1 and GM2 the ductility factor ranges from 3.7 to 3.9 and from 5.2 to 5.5 respectively. Both models can dissipate seismic energy effectively and can be considered as structural systems of medium to high ductility class ["EN 1998-1" 2004].

From the results of the limit analysis and the displacement response to the elastic response spectrum (see section 4.3.1), the corresponding displacement of the SDOF system is higher by

80%, in average, compared to the results of the pushover nonlinear analysis, by means of the N2 method.

5. Conclusions

The seismic vulnerability of the Kuño Tambo church was studied, aiming at reproducing the existing damage patterns and assessing safety under seismic loading. Using pushover nonlinear analyses, tensile crack patterns were obtained and correlated with the observed ones, indicating that the current damage might have been induced partly by past seismic actions. Toe crushing, at horizontal rotation planes, is identified as relevant for the out-of-plane behavior only at post peak and has no hardly influence on the maximum lateral force capacity.

A nonlinear dynamic analysis with artificial accelerograms, under the regional seismic demand, revealed damage patterns, under dynamic loading, in high consistency from both the pushover nonlinear analyses and the documented ones. Yet, in order to quantify the dynamic response and provide accurate statistical response samples, according to site conditions, earthquake sources and the regional design response spectrum, a sufficient number of artificial or natural accelerograms is required, according to provisions from many seismic codes. Despite the apparent different nature of static and dynamic lateral loading, results from dynamic and pushover nonlinear analyses showed identical failure modes. In pushover nonlinear analyses, damage patterns, appear more localized in zones, compared to wider tensile failure distributions, in the dynamic nonlinear analysis. Lateral capacity values in all principal directions are also well correlated, with moderate differences. It is noted that, due to different stiffness characteristics of structural elements, a series of dynamic nonlinear analyses would also need to be performed, with ground motions of increased intensity, in order to obtain maximum capacity values and failure, in all principal directions.

In-situ inspection, together with dynamic and sonic testing, offered valid information regarding the structural behavior, under the current damage and allowed the validation of the current FE model. Results, in terms of maximum lateral capacity and lateral displacements were also correlated with more simplified analytical tools, offering substantial grounds on the assessment process of historic adobe buildings, of similar typology. Limit analysis, with accounted nonlinearity can be considered as an efficient tool for initial structural assessment, especially for accounted values of lateral capacity. Yet, the obtained lateral displacement response assessment is considered rather conservative, compared to results from nonlinear static pushover analysis. In the absence of numerical analysis results, an abacus of all the potential failure mechanisms is necessary, as given in ["OPCM 3431" 2005, "NTC" 2008]. Combined also with engineering judgement and in-situ damage mapping, additional confidence levels can be established and are considered adequate, in terms of lateral capacity values.

The system of tie beams and their connection with the adobe walls of the nave can have a significant effect on the transversal behavior. Under the current condition, given the visual inspection and the results of the dynamic identification tests, the system of ties is considered inactive, especially under the dynamic character of seismic forces.

Two sets of material properties were considered; a less stiff model for properties available in literature and a stiffer model with results obtained from in situ sonic tests. The differences between both are only moderate and the most stringent values were chosen to determine lower bounds of safety. This indicates lower sensitivity of the response to the adopted mechanical data.

One of the structural deficiencies of the church of Kuño Tambo is large asymmetric distribution of stiffness in the transverse direction of the nave. The aligned walls and buttresses along the north wall, when activated through diagonal compression, have a stiffer response. Instead, structural elements of the north front, with lower stiffness characteristics, are engaged

in local failure modes (sacristy gable wall), under low values of lateral seismic loading. The failure mode with the lowest global capacity of 0.19g, is the out-of-plane overturning of the south lateral wall, which controls the response. Thus, strengthening is required, in multiple directions, in order to improve the structural performance, address collapse, during future seismic events and comply with the seismic demand for the Cusco region.

6. Acknowledgements

The current work is part of the Seismic Retrofitting Project, of the Getty Conservation Institute and was partly supported by FCT (Portuguese Foundation for Science and Technology), within the INFRARISK PhD program and ISISE, project UID/ECI/04029/2013.

References

Angelillo M., Lourenço P.B., Milani G. [2014] "Masonry behavior and modelling, Mechanics of Masonry Structures", CISM International Centre for Mechanical Sciences Volume 551, pp 1-26. (DOI:10.1007/978-3-7091-1774-3)

Asteris, P., Chronopoulos, M., Chrysostomou, C., Varum, H., Plevris, V., Kyriakides, N., Silva, V. [2014] "Seismic vulnerability assessment of historical masonry structural systems", Engineering Structures, 62-63, 118-134. (DOI:10.1016/j.engstruct.2014.01.031)

Bowles, J. [1977] "Foundation analysis and design". New York: McGraw-Hill.

Chopra, A. [2001] "Dynamics of Structures: Theory and applications to earthquake engineering", 3rd Edition, Prentice Hall.

Cancino C., Lardinois S., D'Ayala D., Ferreira C.F., Dávila D.T., Meléndez E.V., and Santamato L.V. [2013] "Seismic Retrofitting Project: Assessment of Prototype Buildings", Volume 1 and 2, Getty Conservation Institute, Los Angeles, US. (http://hdl.handle.net/10020/gci_pubs/assess_prototype)

Ciocci, M. P., Sharma, S., & Lourenço, P. B. [2017] "Engineering simulations of a super-complex cultural heritage building: Ica Cathedral in Peru", Meccanica. (DOI:10.1007/s11012-017-0720-3)

DIANA [2014] "TNO DIANA - Manuals" (http://tnodiana.com/DIANA-manuals)

EN 1996-1-1 [2005] “Eurocode 6: Design of masonry structures – Part 1-1: General rules for reinforced and unreinforced masonry structures”, European Committee for Standardization, Brussels, Belgium.

EN 1998-1. [2004] “Eurocode 8: Design of structures for earthquake resistance – General rules, seismic actions and rules for building”, European Committee for Standardization, Brussels, Belgium.

FEMA 306 [1998] “Evaluation of earthquake damaged concrete and masonry wall buildings - Basic Procedures Manual”, Applied Technology Council (ATC-43 Project), ASCE for the Federal Emergency Management Agency, Washington, D.C., US.

FEMA 356 [2000] “Prestandard and Commentary for the Seismic Rehabilitation of Buildings”, ASCE for the Federal Emergency Management Agency, Washington, D.C., US.

Fajfar P. (2000) “A Nonlinear Analysis Method for Performance-Based Seismic Design”, Earthquake Spectra: August 2000, Vol. 16, No. 3, pp. 573-592. (https://doi.org/10.1193/1.1586128)

Franchetti, P. [2014] “Presentation SA3_12: Damage and Collapse Mechanisms in Existing (Particularly Historical) Structures”. SAHC Masters. University of Padova, Italy.

Grau P.N., Neumann J.V., and Beas M. [2006] “Seismic Retrofitting Guidelines for the Conservation of Doctrinal Chapels on the Oyón Highlands in Peru”, Proceedings of the Getty

Seismic Adobe Project 2006, Getty Conservation Institute, Los Angeles, US. (http://hdl.handle.net/10020/gci_pubs/gsap)

Greco F., Karanikoloudis G., Lourenço P.B., Mendes N. [2015] "Experimental In Situ Testing Campaign on Adobe Historic Structures in Peru, within the Getty SR Project", University of Minho, Portugal. (Report 2015-DEC/E-30)

Hilber, H. M., Hughes, T. J. R., Taylor, R. L. [1977] "Improved numerical dissipation for time integration algorithms in structural dynamics." Earthquake Engng. Struct. Dyn., 5: 283–292. (DOI:10.1002/eqe.4290050306)

Lourenço P.B., Mendes N., Ramos L.F., Oliveira D.V. [2011] "On the Analysis of Masonry Structures without box behavior", Taylor & Francis. (http://hdl.handle.net/1822/14786)

Lourenço, P. B. [2002], "Computations on historic masonry structures" Prog. Struct. Engng Mater., 4: 301–319. (DOI:10.1002/pse.120)

Lourenço, P.B. [1996] "Chapter 2: Modelling Masonry: A Material Description" Computational Strategies for Masonry Structures. Delft, Netherlands: Delft UP, 11-26. (uuid:4f5a2c6c-d5b7-4043-9d06-8c0b7b9f1f6f)

Lourenço, P.B. [1998] "Experimental and numerical issues in the modelling of the mechanical behavior of masonry", Structural Analysis of Historical Constructions II: Possibilities of Numerical and Experimental Techniques. Barcelona: International Center for Numerical Methods in Engineering.

Lourenço P.B., Mendes N., Ramos L.F., Oliveira D.V. [2011] “On the Analysis of Masonry Structures without box behavior”, Taylor & Francis. (http://hdl.handle.net/1822/14786)

Lourenço, P.B. [2014] “Presentation SA2_12: Modelling of masonry and homogenization” SAHC Masters. University of Minho, Guimarães, Portugal.

Lumantarna R., Biggs D.T., Ingham J.M. [2014] “Uniaxial Compressive Strength and Stiffness of Field-Extracted and Laboratory-Constructed Masonry Prisms”, ASCE Journal of Materials, Vol 26, No.4, pp.567-575. (DOI:10.1061/(ASCE)MT.1943-5533.0000731)

Mendes, L. [2008] “LNEC-SPA: Signal Processing and Analysis Tools for Civil Engineers”, Earthquake Engineering and Structural Dynamics Division, National Laboratory for Civil Engineering, Lisbon, Portugal.

Mendes, N. [2012] “Seismic assessment of ancient masonry buildings: shaking table tests and numerical analysis” PhD Thesis. University of Minho, Portugal. (http://hdl.handle.net/1822/23110)

NIKER [2010] “New integrated knowledge based approaches to the protection of cultural heritage from earthquake-induced risk, Research Report” University of Padova, Italy.

NTC [2008] “Norme tecniche per le costruzioni” Il Capo del Dipartimento della Protezione Civile. Il Ministro Delle Infrastrutture, Italy (in Italian).

NTE-0.30 [2016] “National Building Code - Technical Standard of building E.030 Earthquake-Resistant Design”, Lima, Peru.

NTE-0.30 [2003] “National Building Code - Technical Standard of building E.030 Earthquake-Resistant Design”, Lima, Peru.

OPCM 3431 [2005] Ordinanza P.C.M. n. 3431 del 3 Maggio 2005, Modification of Ordinanza n. 3274 del 20 Marzo 2003 “General criteria for the seismic zonation of the national territory and technical normative for buildings in seismic zones” (in Italian).

Pereira, J., Lourenço, P.B. [2016] “Numerical Analysis of the SismoAdobe Conference Models from PUPC, Peru, within the Getty SR Project”, University of Minho, Portugal. (Report 2016-DEC/E-019)

Ramos, L. [2007] “Damage identification on masonry structures based on vibration signatures”, PhD Thesis. University of Minho, Portugal. (http://hdl.handle.net/1822/7380)

SRP [2014] “Testing Modeling Report on the SR project” internal report, Getty Conservation Institute, Los Angeles, US.

Stewart, J. P., Chiou, S. J., Bray, J. D., Graves, R. W., Somerville, P. G., Abrahamson, N. A. [2001] “Ground Motion Evaluation Procedures for Performance-Based Design, PEER Report 2001/09”, Pacific Earthquake Engineering Research Center, University of California, Berkeley.

Tarque, N., Camata, G., Spacone, E., Varum, H., & Blondet, M. [2014] “Nonlinear Dynamic Analysis of a Full-Scale Unreinforced Adobe Model”, Earthquake Spectra, 30(4), 1643-1661. (DOI:10.1193/022512eqs053m)

Tembe, S., Lockner, D. A., Wong, T. F. [2010] “Effect of clay content and mineralogy on frictional sliding behavior of simulated gouges: Binary and ternary mixtures of quartz, illite, and montmorillonite” Journal of Geophysical Research, VOL. 115, B03416. (DOI:10.1029/2009JB006383)

Tolles E. L., Kimbro E. E., Webster F. A., Ginell W. S. [1996] “Survey of Damage to Historic Adobe Buildings after the January 1994 Northridge Earthquake”, Getty Conservation Institute, Los Angeles, US.

Tomazevic, M. [1999] “Earthquake-resistance design of masonry buildings”, London: Imperial College Press, cop. 1999.

Trovato, S., Damore, E., Yue, Q., & Spanos, P. [2017] “An approach for synthesizing tri-component ground motions compatible with hazard-consistent target spectrum - Italian aseismic code application”, Soil Dynamics and Earthquake Engineering, 93, 121-134. (DOI: 10.1016/j.soildyn.2016.12.003)

Varum H., Tarque N., Silveira D., Camata G., Lobo B., Blondet M., Figueiredo A., Rafi M. M., Oliveira C. and Costa A. [2014] “Structural Behaviour and Retrofitting of Adobe Masonry Buildings”, Structural Rehabilitation of Old Buildings, Building Pathology and Rehabilitation 2, Springer-Verlag, Berlin Heidelberg. (DOI:10.1007/978-3-642-39686-1_2)

Zanotti S. [2015] “Seismic Analysis of the Church of Kuño Tambo (Peru)”. SAHC Master Thesis, University of Minho, Portugal.

List of Figures

Figure 10. Representation of interface planes between wall intersections and existing discontinuities, in red.

Figure 11. Mode shapes of the first three modes, as obtained from the updated numerical models, in comparison with the modal shapes of the dynamic tests.

Figure 12. Lateral response in all directions, for Models $GM1_{no\text{-}ties}$ and $GM2_{no\text{-}ties}$ and crack pattern at ultimate stage in model $GM1_{no\text{-}ties}$, from lateral loading due to earthquakes: (a) +x-x (E-W); (b) –x-x (W-E), (c) +y-y (N-S), (d) –y-y (S-N).

Figure 13. Minimum principal strain plots, at maximum capacity (left) and toe crushing initiation (right), for Model $GM1_{no\text{-}ties}$: (a) and (b) +x-x (E-W); (c) and (d) +y-y (N-S); (e) and (f) –x-x (W-E); (g) and (h) –y-y (S-N). Note the blue gradient until ultimate compressive strain.

Figure 14. Crack pattern correlation: (a) crack pattern in east façade; (b) crack pattern in the gable wall of baptistery; (c), (d) distribution of principal crack width at collapse (Model $GM1_{no\text{-}ties}$).

Figure 15. (a) Time histories of input signals in east – west and north – south direction; (b) pseudo acceleration response spectrums of EC8 (in black), with the E-W and N-S artificial accelerograms; (c) Rayleigh damping coefficient distribution and frequency bandwidth.

Figure 16. (a) Plots of maximum principal tensile strain scans, in different time steps of the nonlinear dynamic analysis (Model $GM2_{no\text{-}ties}$); (b) superimposed plot of maximum principal tensile strain distribution of all nonlinear pushover analyses (Model $GM2_{no\text{-}ties}$).

Figure 17. Displacements-time histories, in the monitoring points adopted for the nonlinear pushover curves: (a) south lateral wall; (b) west gable wall; (c) sacristy's gable wall; (d) east gable wall.

Figure 18. Dynamic response plots: base shear load factors, superimposed with input acceleration signals in east – west (a) and north – south (b) direction; hysteresis curves of south

lateral wall (c), sacristy gable wall (d), west gable wall (e) and east gable wall (f), with superimposed nonlinear pushover curves.

Figure 19. Rotation of a block around the hinge line, considering a triangular or rectangular distribution of compressive stresses. Note that the maximum stress is different for the two stress blocks.

Figure 20. Limit analysis verification: (a) 3D representation of out-of-plane failure mechanism of the south lateral wall; (b) 3D representation of generic block; (c) out-of-plane rotation of section.

Figure 21. Capacity curve plot, from limit analysis and the Peruvian elastic response spectrum, of the south lateral wall.

Figure 22. South lateral wall: (a) Out-of-plane failure mode representation and discretized zones; (b) normalized plots of lateral deformed shapes, during the evolution of lateral loads, for models GM1 and GM2 without ties (note intermediate deformed shape trajectories in grey).

Figure 23. (a) Elastic response spectrum and idealized capacity curves of the SDOF system; (b) capacity curves for models GM1 and GM2 without ties in MDOF and SDOF configuration.

(a) (b)

Figure 1. Kuño Tambo church: (a) aerial view [Cancino et al. 2013]; (b) 3D CAD model (light grey), with the highlight of various openings in red and the base masonry course (dark grey).

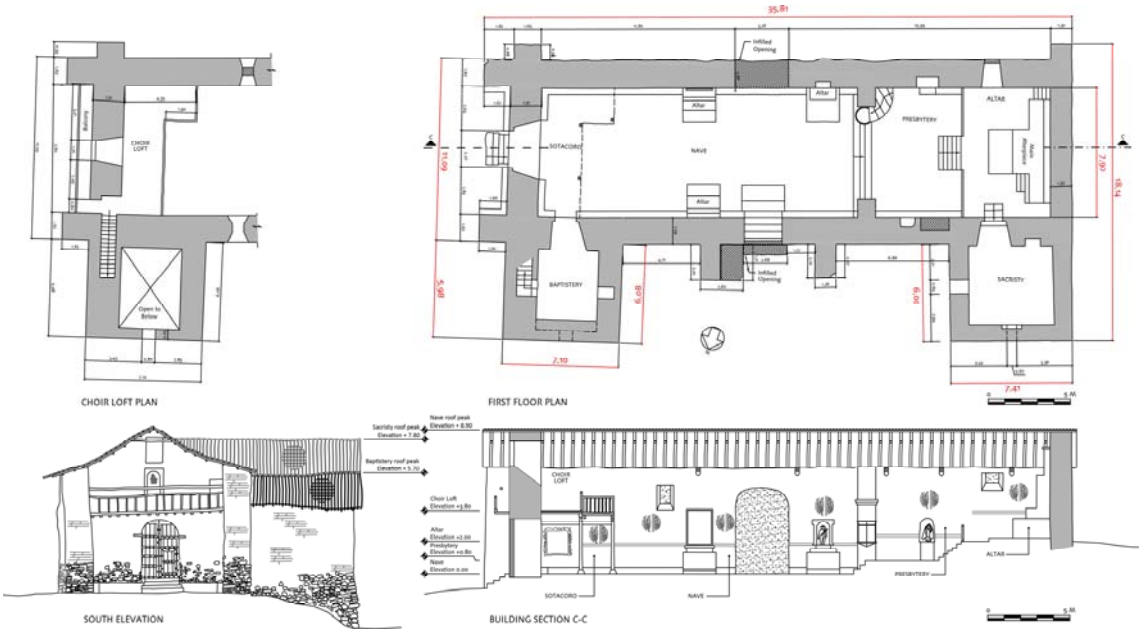

Figure 2. Architectural plans and elevations (North indication in main plan) [Cancino et al. 2013].

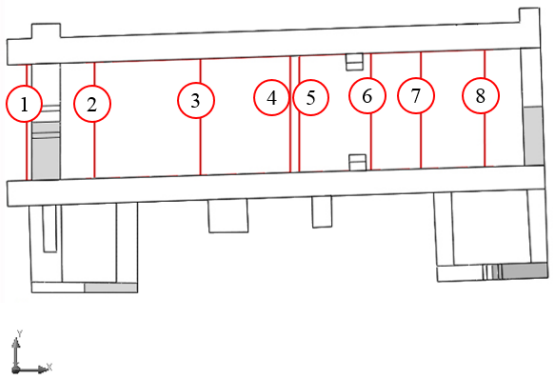

Figure 3. Representation of timber tie beams in plan view.

Figure 4. Damage maps in each facade [Zanotti 2015].

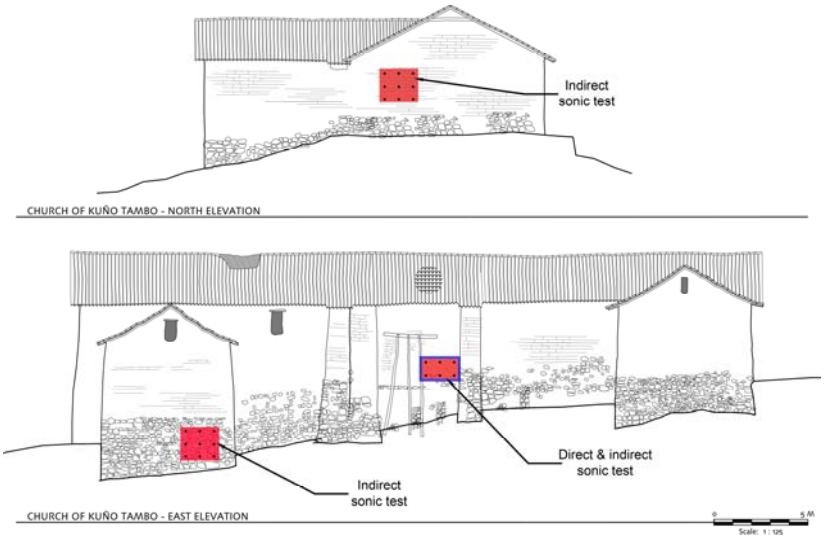

Figure 5. Location of direct (blue) and indirect (red) sonic tests in adobe and rubble stone masonry [Cancino et al. 2013].

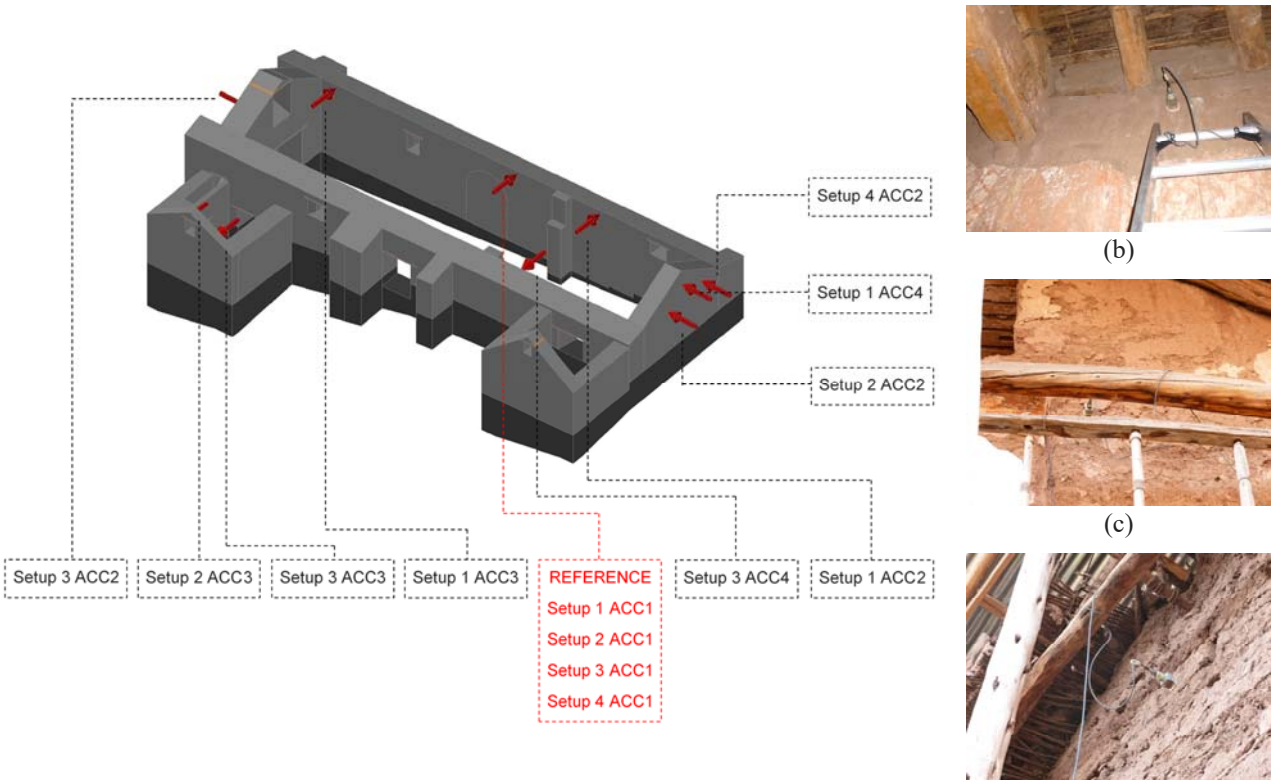

(a)

(b)

(c)

(d)

Figure 6. (a) Disposition of accelerometers in the performed setups at the nave and baptistery walls; (b) accelerometer near the wall plate of the south lateral wall, (c) accelerometer on the exterior cladding of the east facade, (d) accelerometer on the exterior cladding of the west façade.

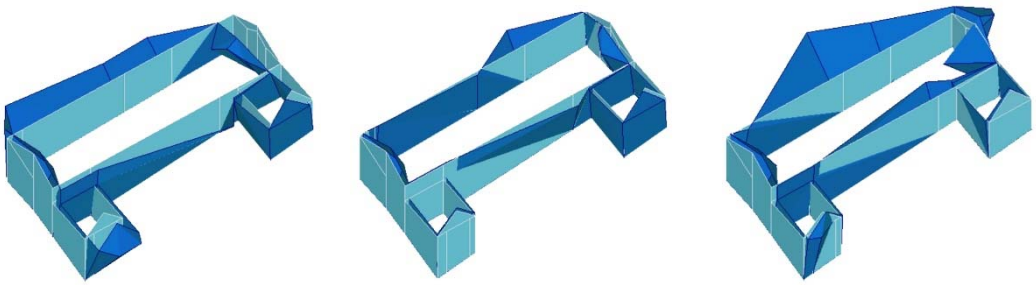

Mode 1 (1.59 Hz) Damping=0.71%

Mode 2 (2.15 Hz) Damping=3.67%

Mode 3 (2.68 Hz) Damping=0.63%

Figure 7. Mode shapes from the dynamic tests, obtained with the SSI-UPC Method, of the first three modes, with interpolation [Zanotti 2015].

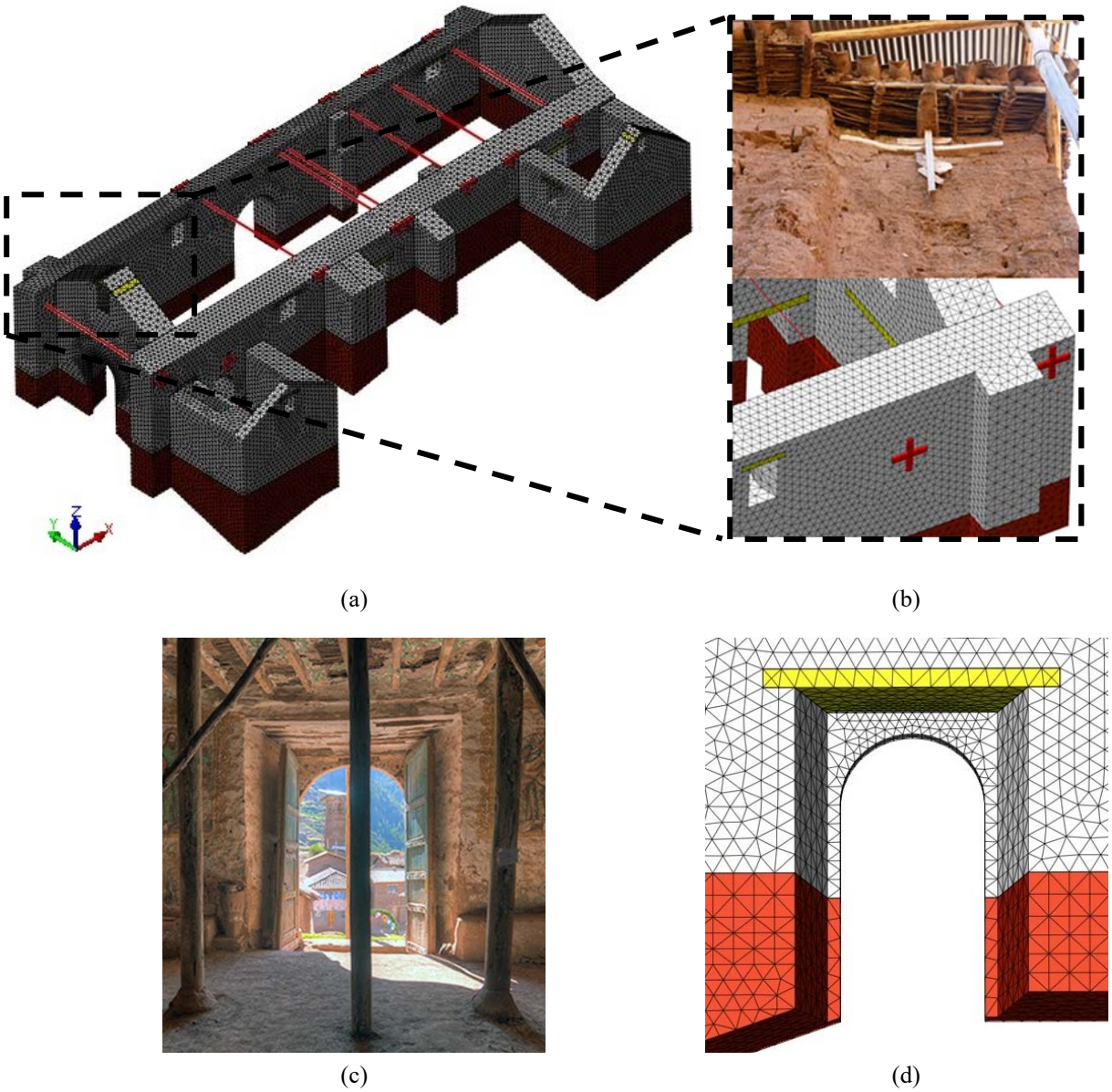

Figure 8. (a) 3D view of the FE model with base course foundation in brown and ties in red; (b top) timber anchor on the southeast corner of the lateral wall; (b bottom) closer view of the timber anchors and their connectivity in the south adobe wall; (c) interior view of the main entrance; (d) modelling of the entrance of the nave.

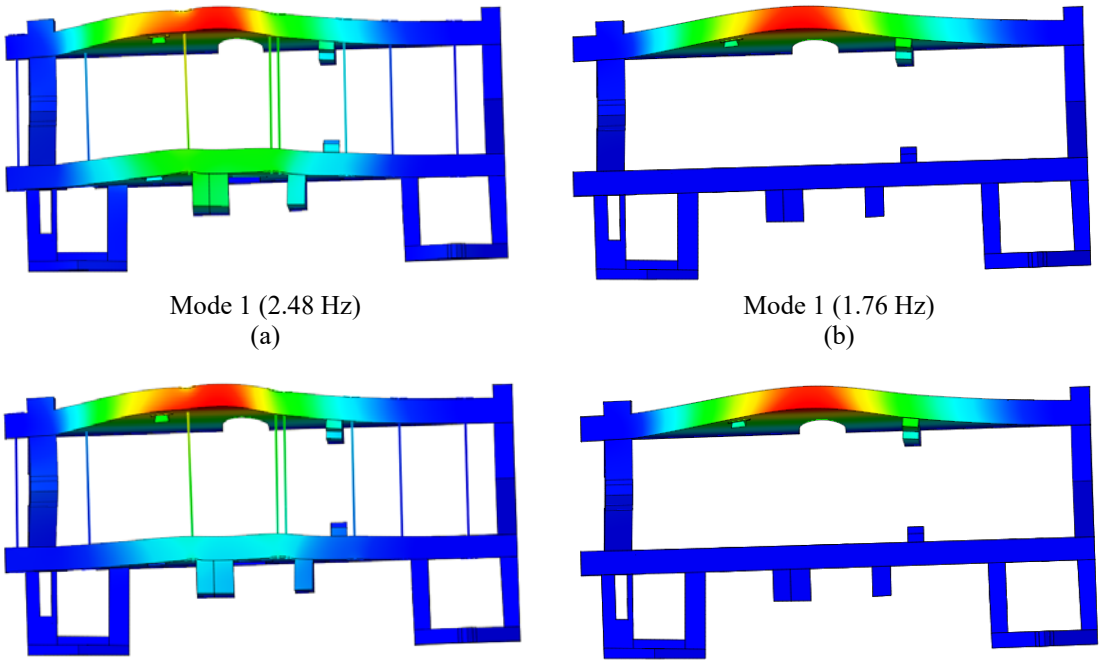

Mode 1 (2.48 Hz)
(a)

Mode 1 (1.76 Hz)
(b)

Mode 1 (4.11 Hz)
(c)

Mode 1 (3.02 Hz)
(d)

Figure 9. Mode shape configuration of the 1st translational mode: model GM1 (material properties from literature) with the presence of ties (a) and without the presence of ties (b); model GM2 (material properties from sonic tests) with the presence of ties (c) and without the presence of ties (d).

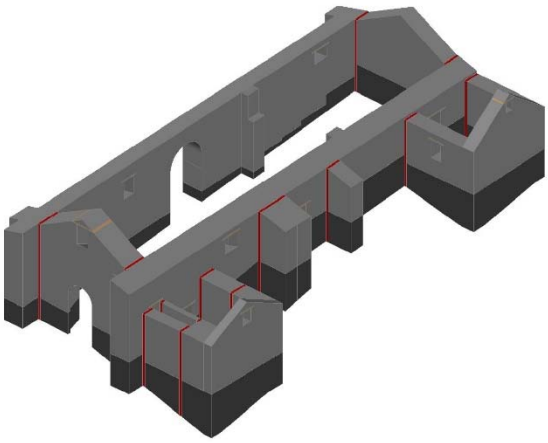

Figure 10. Representation of interface planes between wall intersections and existing discontinuities, in red.

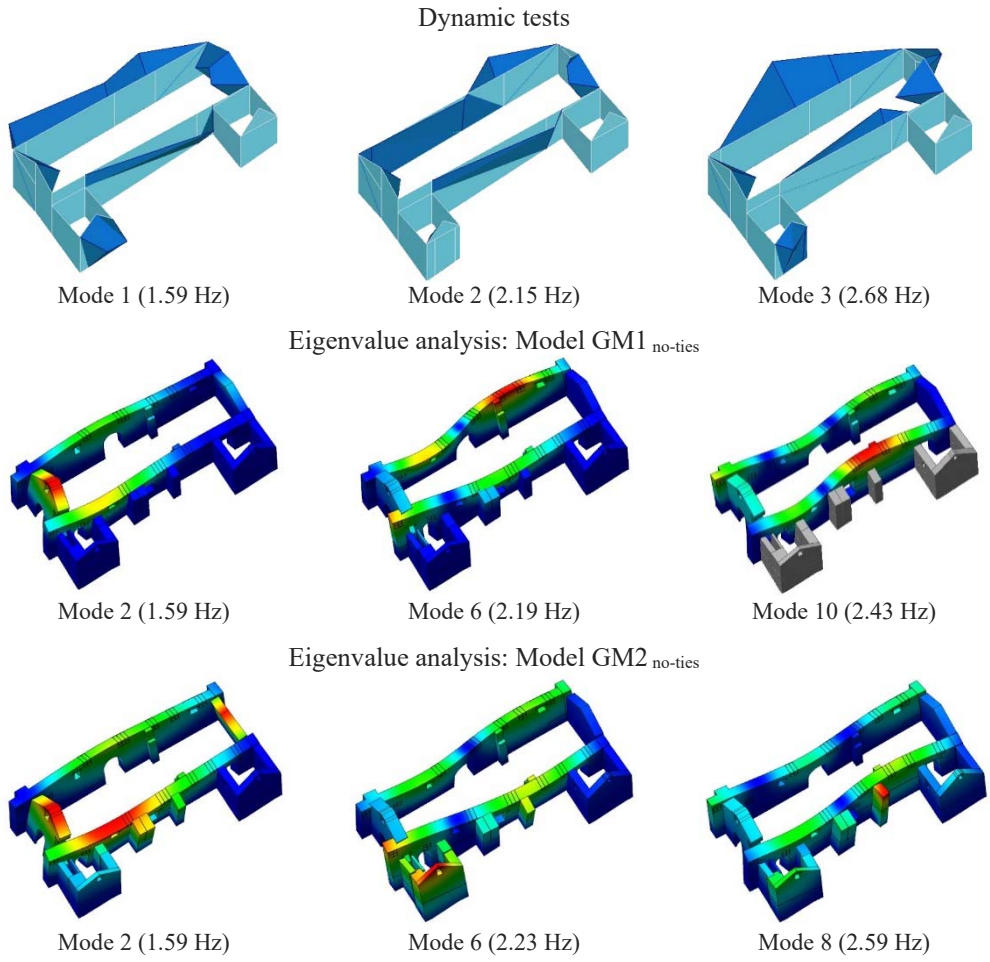

Figure 11. Mode shapes of the first three modes, as obtained from the updated numerical models, in comparison with the modal shapes of the dynamic tests.

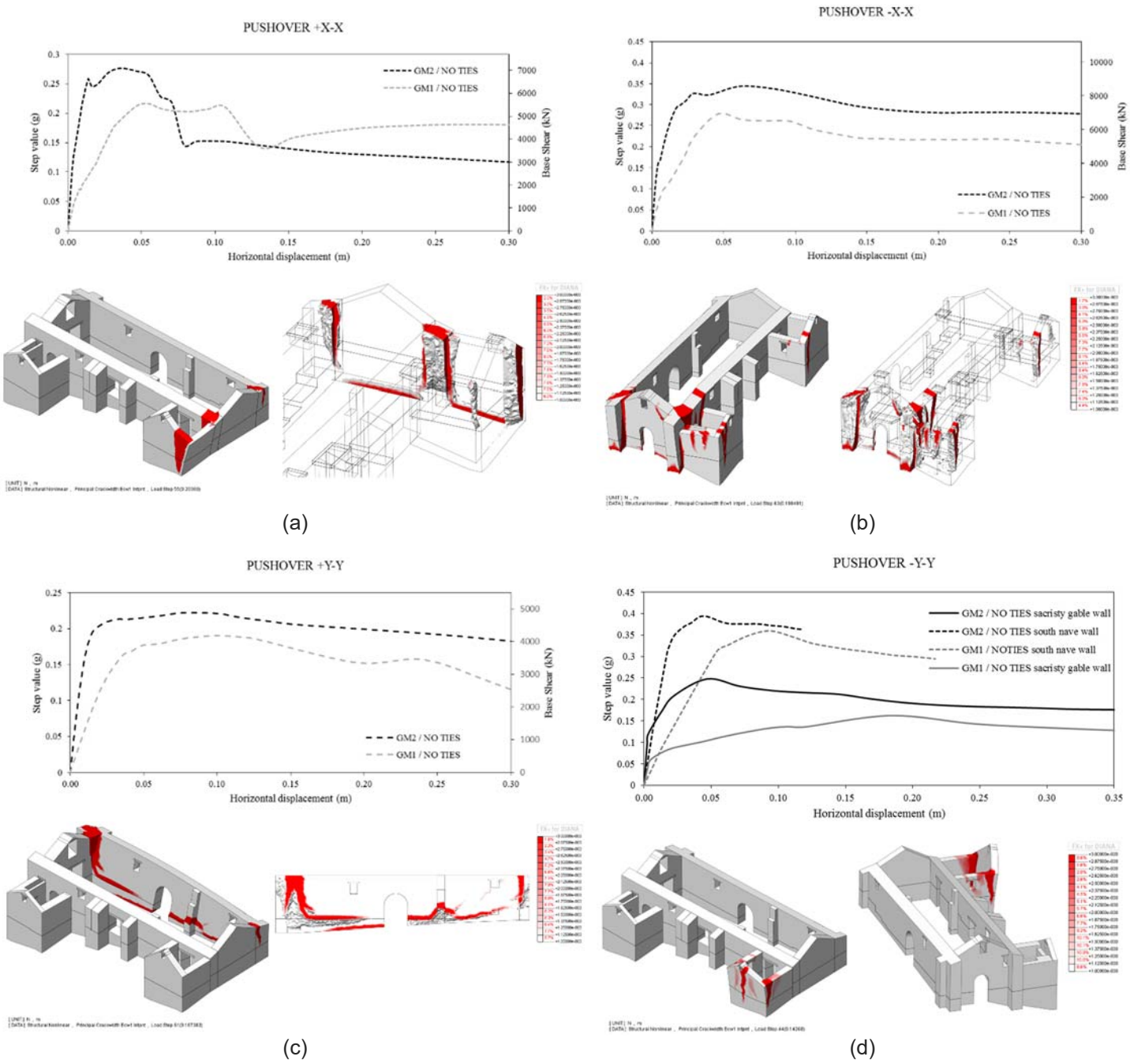

Figure 12. Lateral response in all directions, for Models $GM1_{no\text{-}ties}$ and $GM2_{no\text{-}ties}$ and crack pattern at ultimate stage in model $GM1_{no\text{-}ties}$, from lateral loading due to earthquakes: (a) +x-x (E-W); (b) –x-x (W-E), (c) +y-y (N-S), (d) –y-y (S-N).

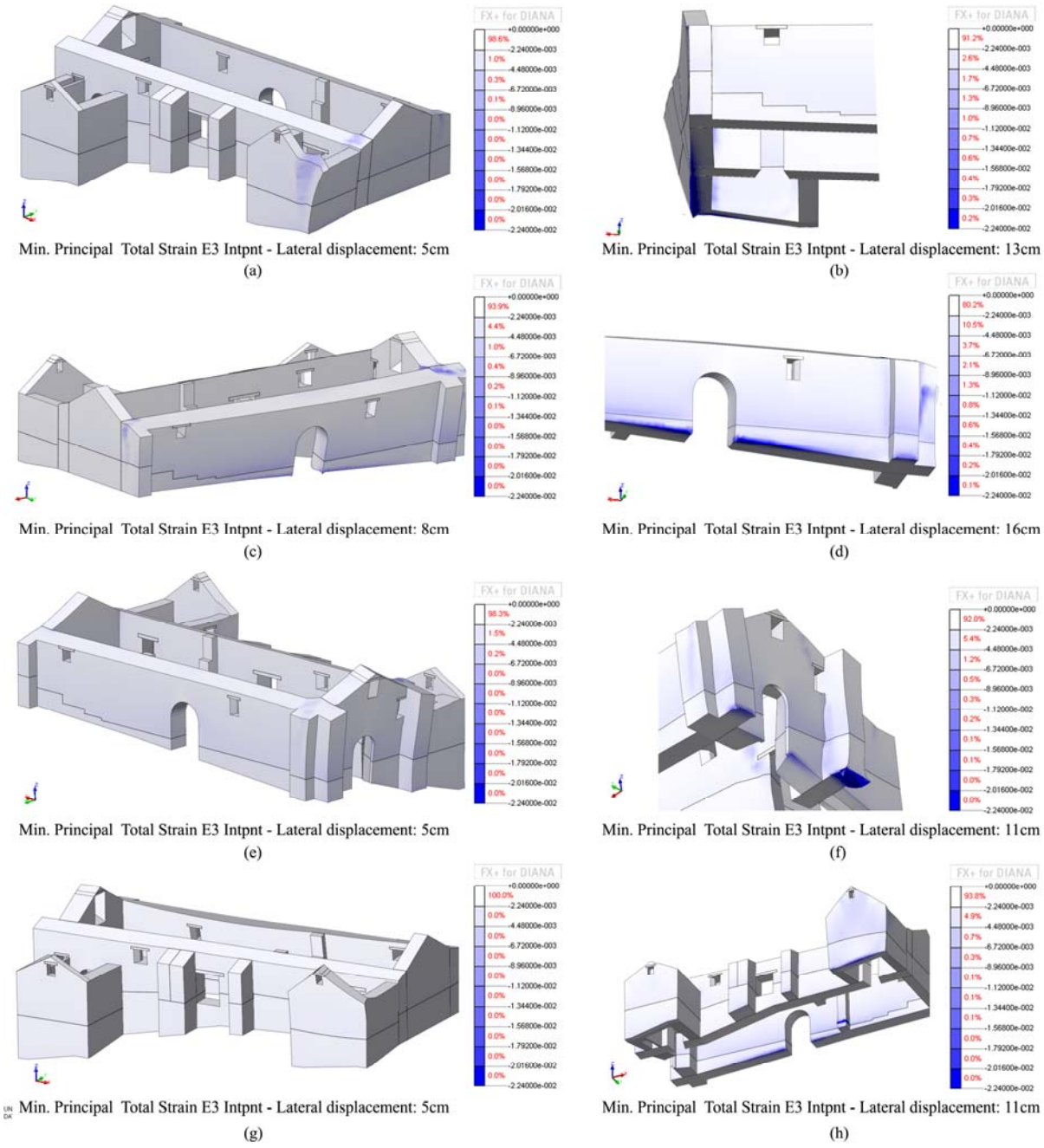

Figure 13. Minimum principal strain plots, at maximum capacity (left) and toe crushing initiation (right), for Model $GM1_{no\text{-}ties}$: (a) and (b) +x-x (E-W); (c) and (d) +y-y (N-S); (e) and (f) –x-x (W-E); (g) and (h) –y-y (S-N). Note the blue gradient until ultimate compressive strain.

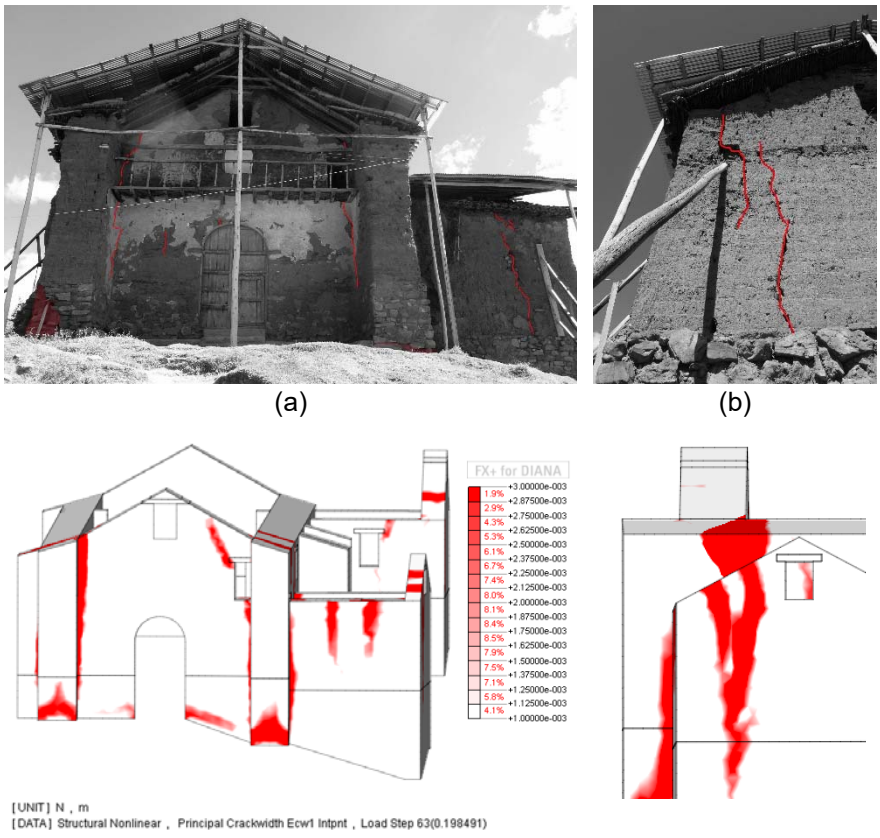

Figure 14. Crack pattern correlation: (a) crack pattern in east façade; (b) crack pattern in the gable wall of baptistery; (c), (d) distribution of principal crack width at collapse (Model $GM1_{no\text{-}ties}$).

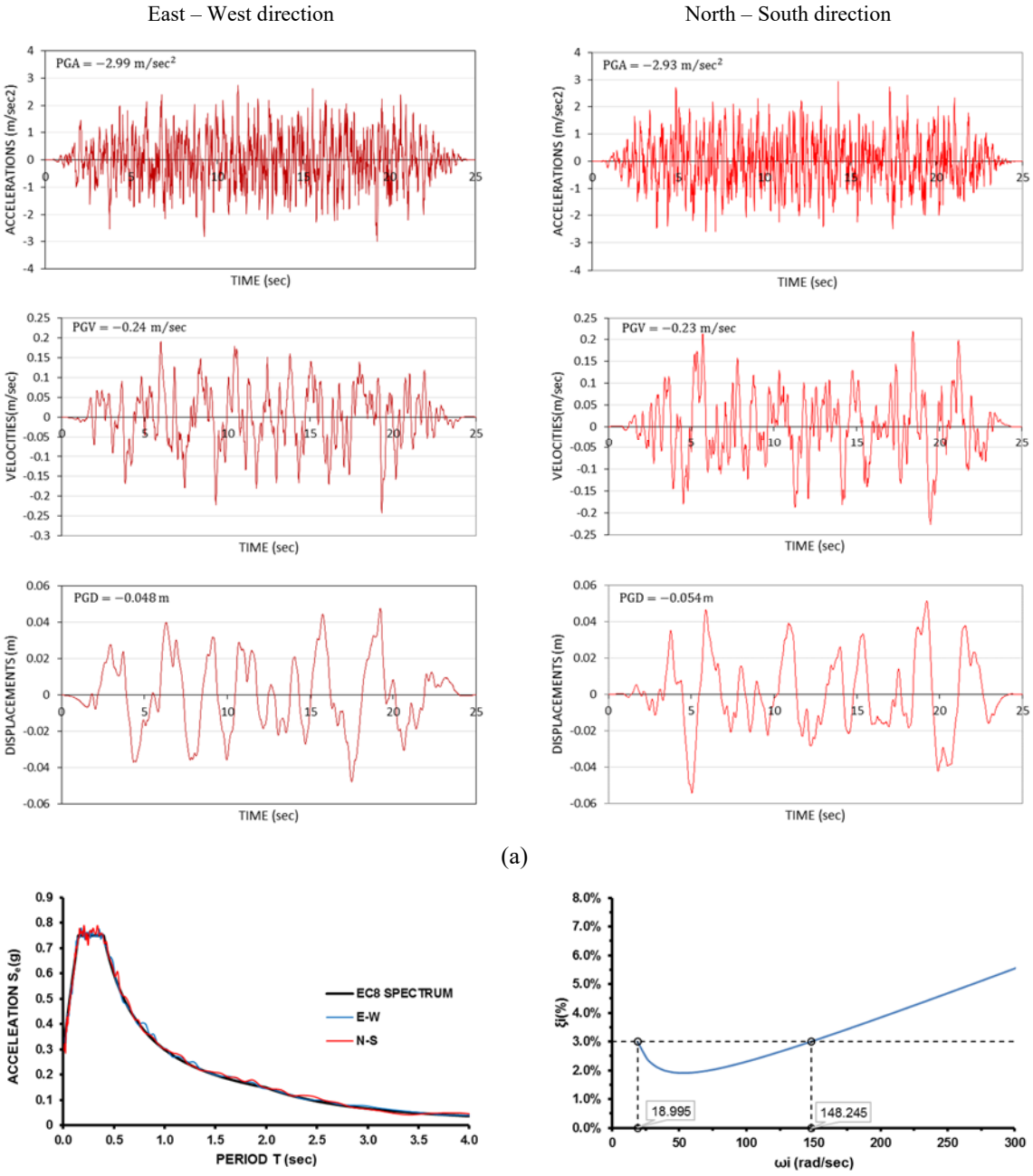

Figure 15. (a) Time histories of input signals in east – west and north – south direction; (b) pseudo acceleration response spectrums of EC8 (in black), with the E-W and N-S artificial accelerograms; (c) Rayleigh damping coefficient distribution and frequency bandwidth.

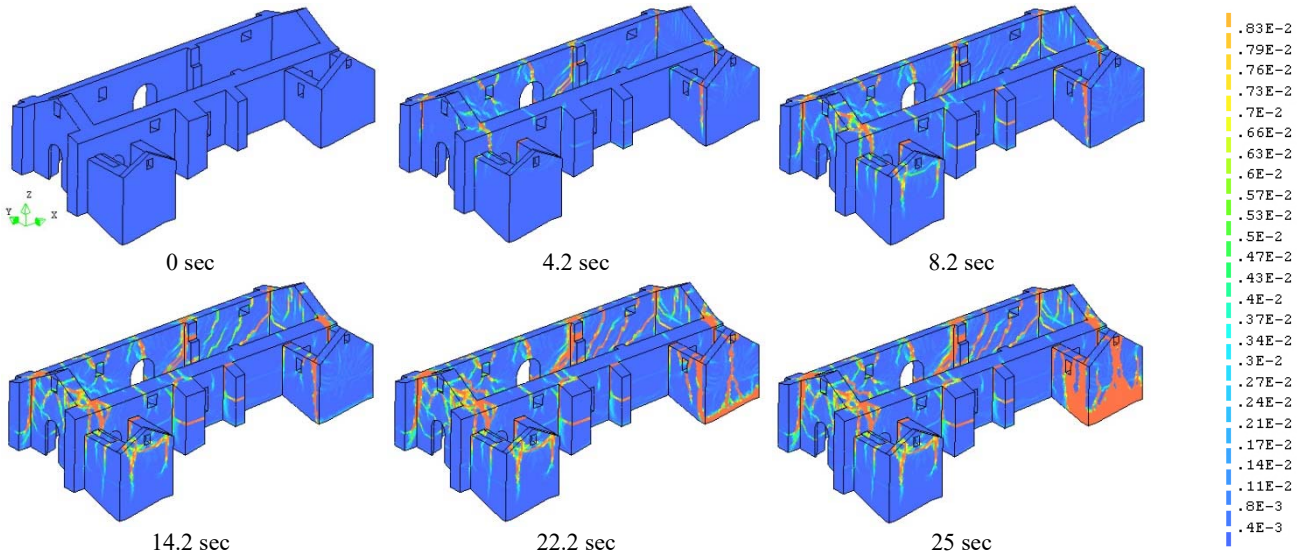

(a)

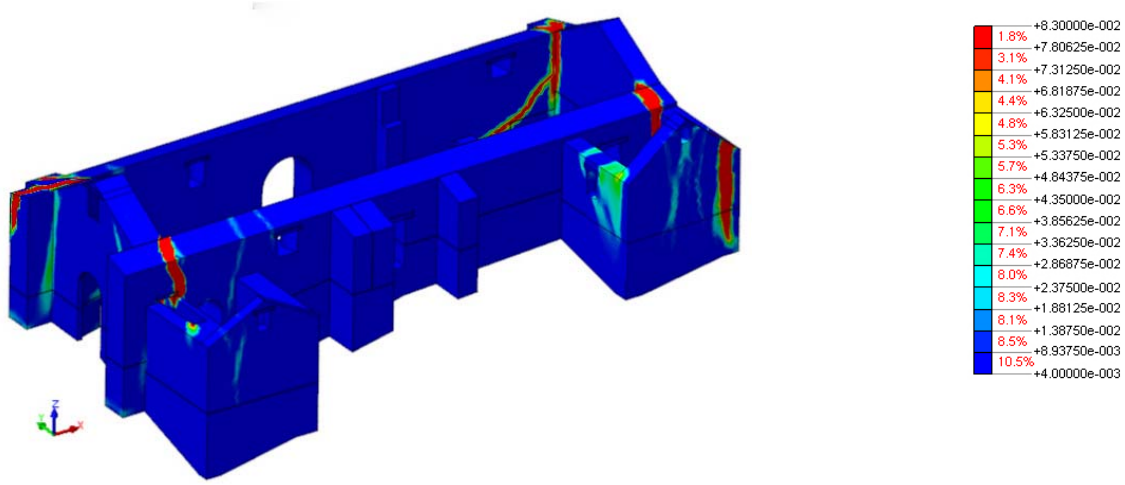

(b)

Figure 16. (a) Plots of maximum principal tensile strain scans, in different time steps of the nonlinear dynamic analysis (Model $GM2_{no\text{-}ties}$); (b) superimposed plot of maximum principal tensile strain distribution of all nonlinear pushover analyses (Model $GM2_{no\text{-}ties}$).

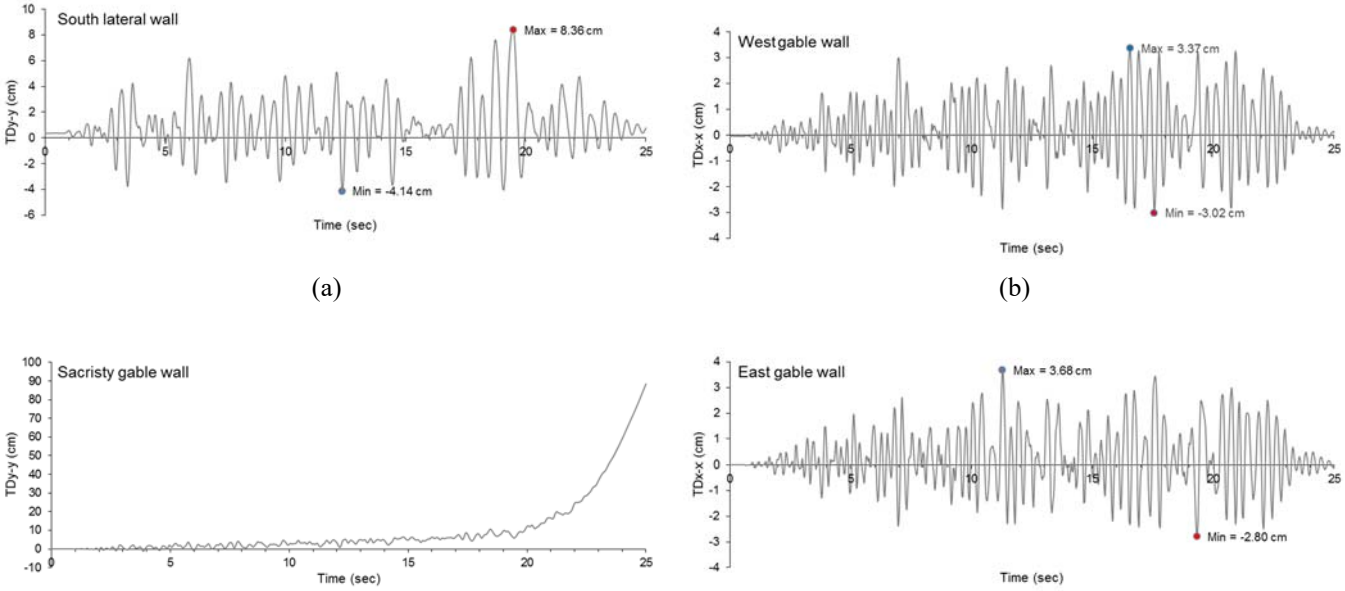

Figure 17. Displacements-time histories, in the monitoring points adopted for the nonlinear pushover curves: (a) south lateral wall; (b) west gable wall; (c) sacristy's gable wall; (d) east gable wall.

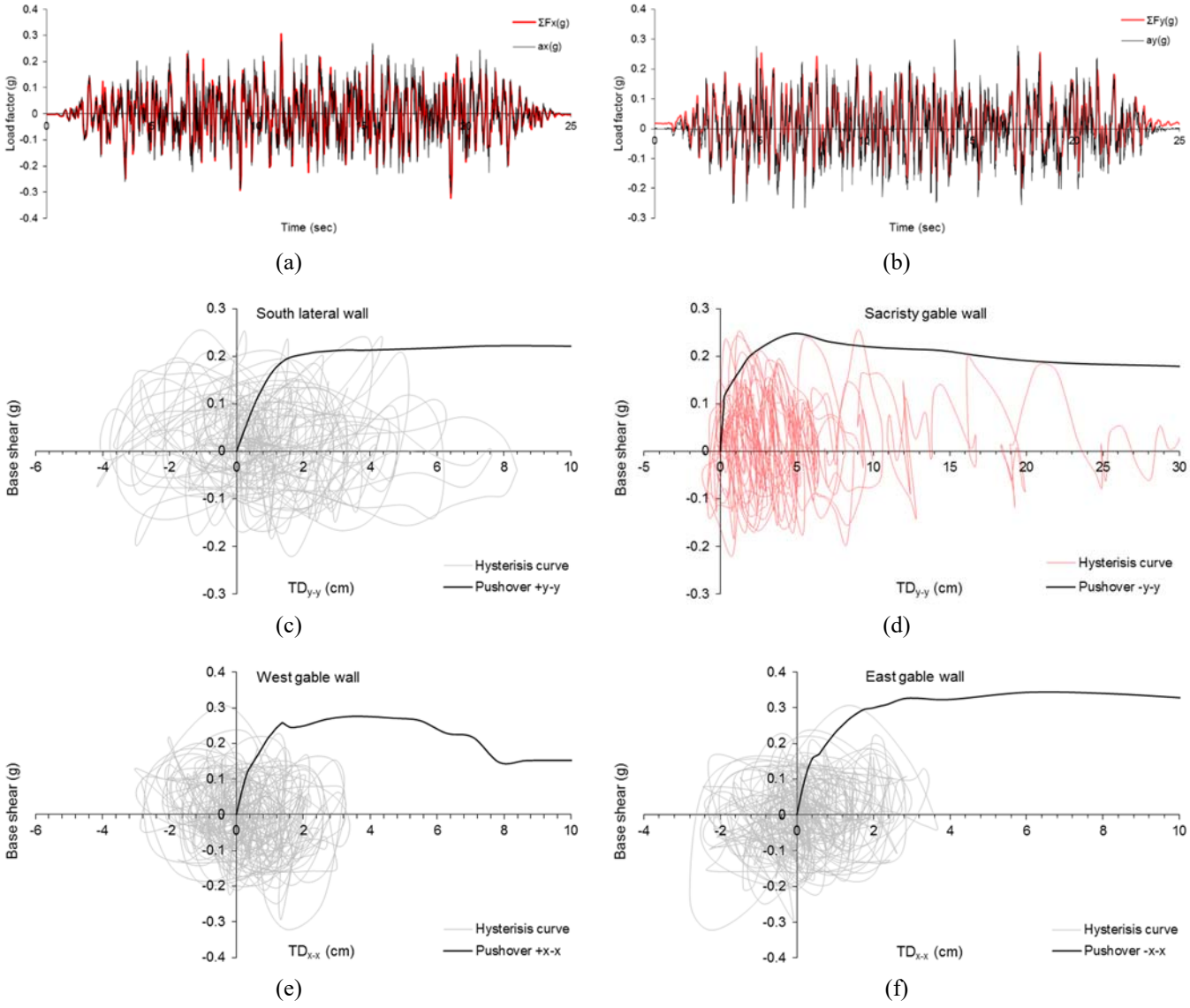

Figure 18. Dynamic response plots: base shear load factors, superimposed with input acceleration signals in east – west (a) and north – south (b) direction; hysteresis curves of south lateral wall (c), sacristy gable wall (d), west gable wall (e) and east gable wall (f), with superimposed nonlinear pushover curves.

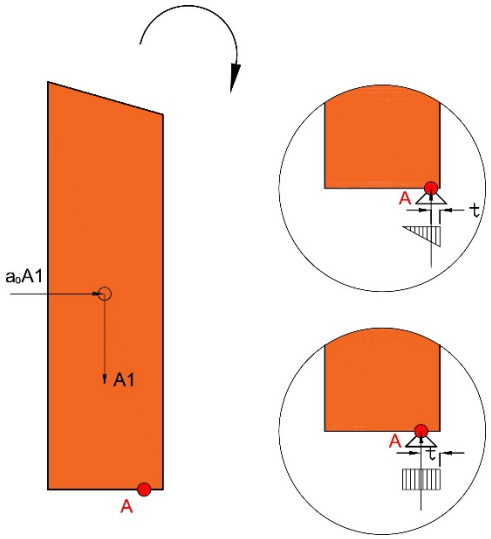

Figure 19. Rotation of a block around the hinge line, considering a triangular or rectangular distribution of compressive stresses. Note that the maximum stress is different for the two stress blocks.

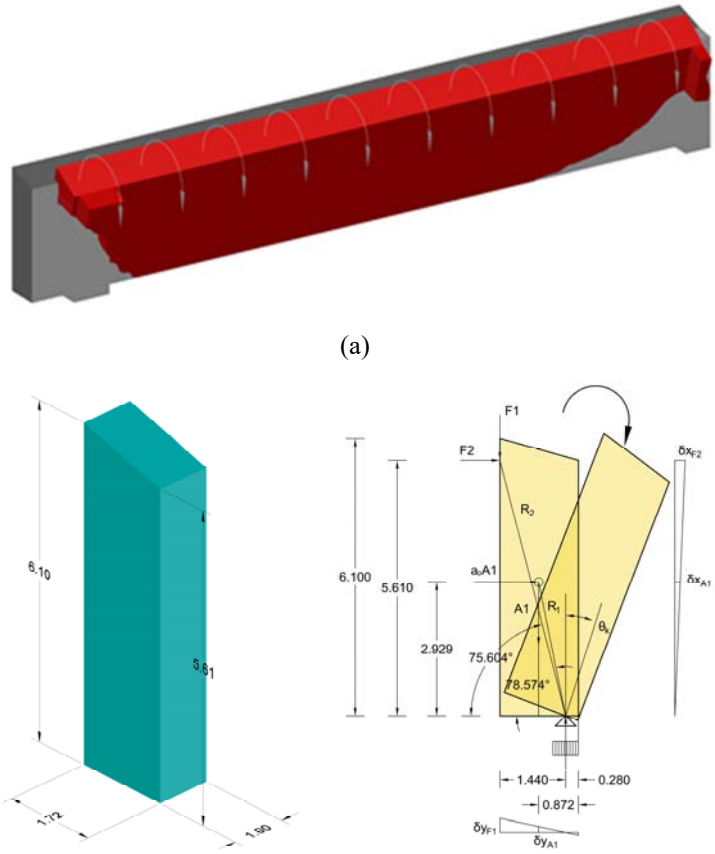

Figure 20. Limit analysis verification: (a) 3D representation of out-of-plane failure mechanism of the south lateral wall; (b) 3D representation of generic block; (c) out-of-plane rotation of section.

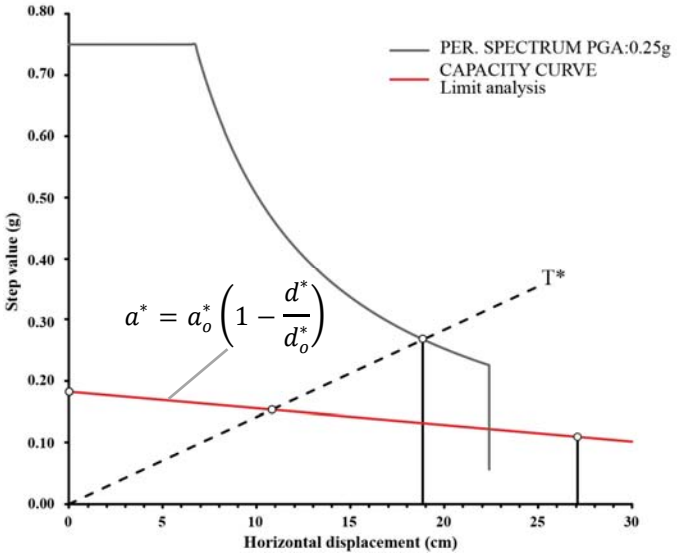

Figure 21. Capacity curve plot, from limit analysis and the Peruvian elastic response spectrum, of the south lateral wall.

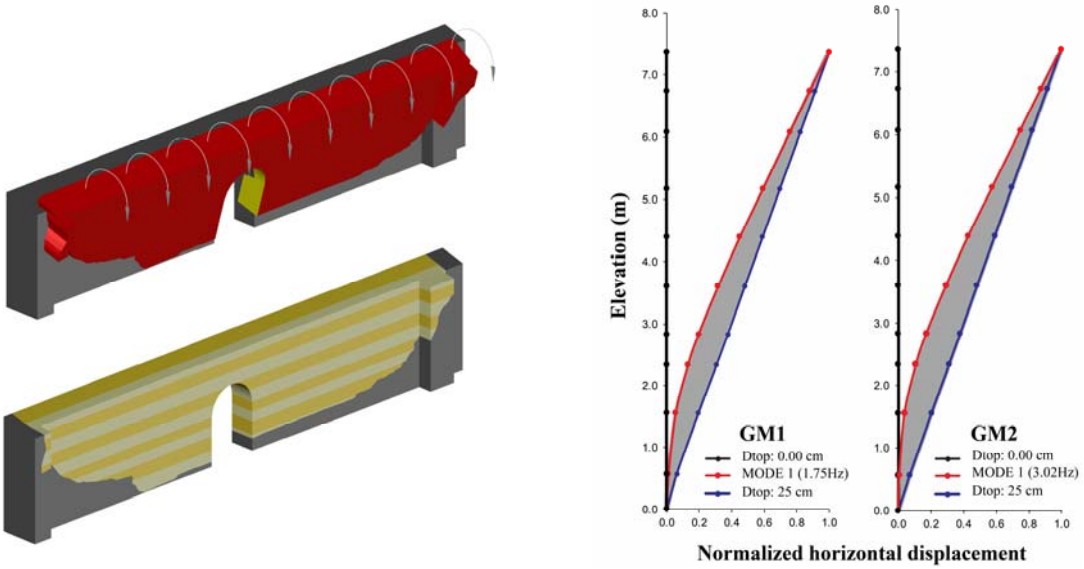

(a) (b)

Figure 22. South lateral wall: (a) Out-of-plane failure mode representation and discretized zones; (b) normalized plots of lateral deformed shapes, during the evolution of lateral loads, for models GM1 and GM2 without ties (note intermediate deformed shape trajectories in grey).

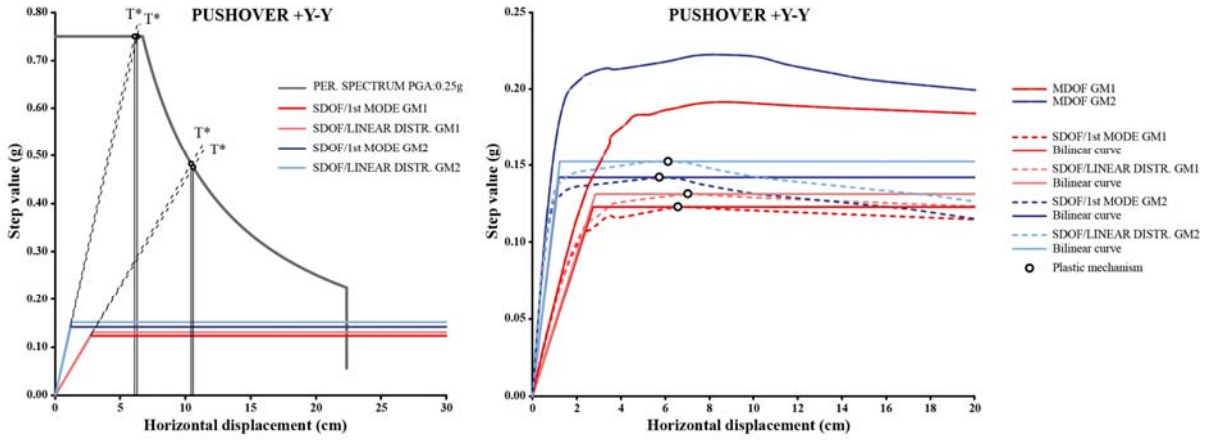

(a) (b)

Figure 23. (a) Elastic response spectrum and idealized capacity curves of the SDOF system; (b) capacity curves for models GM1 and GM2 without ties in MDOF and SDOF configuration.

List of tables

Table 1. Mechanical properties of adobe masonry and rubble stone masonry.

Mechanical properties		Adobe masonry	Rubble stone masonry
Compressive strength	f_c (MPa)	0.45	0.60[4]
Modulus of elasticity	E (MPa)	100[1] / 270[2]	300[4] / 1570[2]
$\alpha = E_m/f_c$	-	222/600	500/2617
Poisson's ratio	v (-)	0.2	0.2
Tensile strength	f_t (MPa)	0.05	0.06
Fracture energy Mode I (tension)	G_f (N/mm)	0.01	0.01
Fracture energy (compression)	G_c (N/mm)	1.0	1.5
Specific weight	ρ (kN/m^3)	19[3]	19[4]

[1] Literature review, [2] Sonic tests, [3] Vecchi, S.S. (2009) Peru, [4] Table 11.D.1 of OPCM 3431, 2005

Table 2. Mechanical properties of timber elements.

Properties	Lower	Higher
Basic density (g/cm^3)	0.40	0.49
Moisture content at the time of testing (%)	17	16
Elasticity modulus in bending, MOE (x1000 MPa)	7.8	10.7
Flexural strength parallel to grain (MPa)	61.5	75.8
Compressive strength parallel to grain (MPa)	33.4	38.1
Compressive strength perpendicular to grain (MPa)	4.7	6.3
Shear strength parallel to grain (MPa)	6.3	10.1
Tensile strength parallel to grain (MPa)	47.8	64.1
Tensile strength perpendicular to grain (MPa)	1.6	1.8

Table 3. Stiffness values for springs and interfaces, in the updated numerical models.

			Interfaces									
	Springs at base		East façade		West façade		Sacristy		Buttresses		Baptistery	
	K_z (N/mm)	$K_{x,y}$ (N/mm)	K_n (N/mm^3)	K_s (N/mm^3)	K_n (N/mm^3)	K_s (N/mm^3)	K_n (N/mm^3)	K_s (N/mm^3)	K_n (N/mm^3)	K_s (N/mm^3)	K_n (N/mm^3)	K_s (N/mm^3)
$GM1_{no\text{-}ties}$	21000	8400	0.0022	0.0014	0.0022	0.0012	0.0022	0.0012	0.0001	0.0008	0.0001	0.0008
$GM2_{no\text{-}ties}$	2900	1160	0.0022	0.0011	0.0022	0.0012	0.0022	0.0012	0.0022	0.0011	0.0022	0.0011

Table 4. Load calculation in generic block.

	E (m^2)	L (m)	V (m^3)	Wi (kN)	x_{Gi}	y_{Gi}	$\delta_{x,i}$	$W_i*\delta_{x,i}$	$W_i*\delta_{x,i}^2$	β_{Gi}^o	R_i (m)	W_i*R_i
A1	10.07	1.00	10.07	191.34	0.87	2.93	0.52	99.90	52.16	78.57	2.99	571.80
F1	-	1.00	-	10.52	1.72	5.61	1.00	10.52	10.52	75.60	5.79	60.91
F2	-	1.00	-	5.32	1.72	5.61	-	-	-	-	-	-